Contents lists available at ScienceDirect

Bioactive Materials

Treatment of critical bone defects using calcium phosphate cement and mesoporous bioactive glass providing spatiotemporal drug delivery

Richard Frank Richter [a], Corina Vater [a], Margarete Korn [b], Tilman Ahlfeld [a], Martina Rauner [c], Winnie Pradel [b], Bernd Stadlinger [d], Michael Gelinsky [a], Anja Lode [a], Paula Korn [a,b,*]

[a] Centre for Translational Bone, Joint and Soft Tissue Research, University Hospital Carl Gustav Carus and Faculty of Medicine, Technische Universität Dresden, Dresden, Germany
[b] Department of Oral and Maxillofacial Surgery, University Hospital Carl Gustav Carus, Technische Universität Dresden, Germany
[c] Department of Medicine III and Center for Healthy Aging, University Hospital Carl Gustav Carus, Technische Universität Dresden, Germany
[d] Clinic of Cranio-Maxillofacial and Oral Surgery, Center of Dental Medicine, University of Zurich, Switzerland

ARTICLE INFO

ABSTRACT

Calcium phosphate cements (CPC) are currently widely used bone replacement materials with excellent bioactivity, but have considerable disadvantages like slow degradation. For critical-sized defects, however, an improved degradation is essential to match the tissue regeneration, especially in younger patients who are still growing. We demonstrate that a combination of CPC with mesoporous bioactive glass (MBG) particles led to an enhanced degradation *in vitro* and in a critical alveolar cleft defect in rats. Additionally, to support new bone formation the MBG was functionalized with hypoxia conditioned medium (HCM) derived from rat bone marrow stromal cells. HCM-functionalized scaffolds showed an improved cell proliferation and the highest formation of new bone volume. This highly flexible material system together with the drug delivery capacity is adaptable to patient specific needs and has great potential for clinical translation.

1. Introduction

Critical-sized bone defects can occur due to manifold causes for example traumata, systemically diseased bone, congenital malformation or surgical resection of infectious or tumorous tissue. The treatment of such defects is challenging. The gold standard is the use of autologous bone grafts which has several disadvantages like limited availability, the need of an additional surgical procedure for the tissue extraction and donor site morbidity [1]. Filling of bone defects with synthetic biomaterials may be an alternative as they can stabilize the defect and support bone regeneration. In general, a synthetic material that promotes tissue regeneration should be biocompatible, biodegradable and able to deliver cell-inducing stimuli [2]. Critical size defects in growing organisms are challenging, because on one hand the above mentioned criteria should be fulfilled and on the other hand the resorption characteristics of the biomaterial needs to be adapted to the rate of bone and tissue growth. One example are alveolar clefts, which occur in approximately 70% of all human clefts [3]. There is a clinical need to refine the current therapy and patient-specific, biodegradable, osteoconductive

scaffolds might be a promising strategy.

Calcium phosphate cements (CPC) are one example for a bone replacement material system that is widely investigated and is already used in clinical applications as it fulfils the general requirements mentioned above. Typically, self-setting CPC consist of a liquid phase and at least one calcium phosphate (CaP) precursor with hydraulic reactivity like α-tricalcium phosphate (α-TCP) [4]. After contact with aqueous media, these CPC immediately start self-induced dissolution-precipitation reactions and form non-stoichiometric, nanocrystalline, calcium-deficient hydroxyapatite (CDHA) at neutral pH that is resorbable by osteoclasts [5,6]. Commonly, these CPC are applied as moldable pastes, which get prepared within the operating theatre by mixing the precursor powder with an aqueous liquid and have to be injected into the bone defect quickly. Thus, powder/liquid-cements (p/l-CPC) only have a short processing time because of the immediately starting setting reaction which will impair the extrudability of the cement through a needle. Therefore, p/l-CPC are limited in their applicability as injectable bone replacement material and several studies investigated the possibility to retard the setting reaction to increase the

processing time, for example by mixing the α-TCP-based precursors with gelatine or Pluronic 127 [7–9].

An effective strategy is the combination of CaP precursors with a water-immiscible, biocompatible oil-based carrier liquid (cl), which is exchanged with water during setting of the CPC [10]. Until this cl-CPC is exposed to an aqueous environment, the setting reaction is completely prevented and therefore allows infinite extrusion through nozzles with high reproducibility. As a result, such cl-CPC formulations are applicable for extrusion-based additive manufacturing at low-temperature (called 3D plotting) [11], allowing the fabrication of patient/defect specific, anatomically shaped three-dimensional constructs [12,13]. The mild fabrication conditions provide the possibility to combine the cl-CPC with sensitive biological components (e.g. protein, growth factors), loaded on carrier materials, resulting in a drug delivery system [14]. Additionally, p/l- and cl-CPC themselves can be easily modified by incorporation of inorganic bone stimuli like strontium ions [15–17]. Strontium is of particular interest for bone regeneration as it was demonstrated that Sr^{2+} ions accelerate osteogenic differentiation but decelerate osteoclastic resorption [18–21]. Besides these advantageous properties, a major disadvantage of the CPC in general though is its slow degradation and resorption in vivo [12,16,22].

A promising strategy to overcome this drawback is the integration of another, faster degrading material into the CPC leading to an increased porosity over time followed by enhanced degradation of the CPC matrix. A suitable material could be mesoporous bioactive glass (MBG). Silicate based bioglasses are known for their excellent biocompatibility, similar to CaP, and formation of stable bonds to bone and soft tissue [23]. MBG are typically synthesised via sol-gel methods and possess a highly ordered intrinsic pore structure and a high specific surface area (200–500 m^2/g) [24]. Due to their structure and the chemically-based degradation process, they degrade much faster in a physiological environment than CDHA [25,26]. With this high surface area, MBG are also an excellent carrier material for biomolecules, as they additionally possess a high binding affinity for proteins and the high surface area therefore translates into a high binding capacity [24]. Based on a p/l-CPC, Schumacher et al. developed a CPC-MBG composite and demonstrated in vitro that the incorporation of MBG particles not only allowed controlled growth factor delivery (after loading with vascular endothelial growth factor - VEGF), but also led to an improved degradation and therefore higher porosity after immersion in water for 21 days [27].

Building on these promising results, we recently developed CPC-MBG composites based on the cl-CPC that are also suitable for 3D plotting. They showed the superiority of 3D plotted, macroporous scaffolds compared to bulk constructs in terms of degradation and ion release due to their higher surface-to-volume ratio [28]. Moreover, we developed a protocol that allows the incorporation of protein- or growth factor-laden MBG particles into the CPC paste whereby the plottability was not impaired and the released biomolecules still maintained their biological activity [29]. This opens up a highly flexible material toolbox, as scaffolds cannot only be manufactured in defect- and thus patient-specific shape and size, the release of therapeutically active agents can be tailored in a defined spatiotemporal manner to fit patient-individual needs as well.

With this toolbox at hand, we fabricated in the present study scaffolds by 3D plotting of a functionalized CPC-MBG composite and tested them in an in vivo application. The defect model selected was an established rat model for alveolar cleft osteoplasty, because cleft defects are the most common congenital craniofacial anomalies in humans with a prevalence of about 1 per 700 live birth [30,31]. The established procedure for secondary alveolar cleft osteoplasty, implantation of an autogenous iliac bone graft, suffers from the before mentioned typical drawbacks [31–33] and an appropriate synthetic material system could help to improve the treatment quality for those young patients, because harvesting autologous bone grafts would not be necessary anymore.

In a previous study we investigated 3D plotted CPC constructs with and without cell seeding prior to implantation in this defect model. We

confirmed the excellent osteoconductivity of the CPC, but also observed a slow degradation and no benefit of pre-colonized scaffolds [12]. Furthermore, a general problem of such classical tissue engineering constructs remains, which is the insufficient supply of the pre-seeded cells after implantation due to the lack of vascularization that often led to no significant improvements of these constructs [12,34,35]. A potential solution is the approach of in situ tissue engineering in which the scaffolds have the intrinsic ability to recruit cells with regenerative potential from the surrounding tissue because of the release of chemotactic factors; the cells migrate only as far into the scaffolds as they are still sufficiently supplied and this process is supported by simultaneous ingrowth of blood vessels [34,35]. In the present study, we therefore investigated a CPC-MBG composite in which the MBG particles were loaded with a complex protein mixture derived from hypoxia conditioned medium (HCM). As hypoxia mimics the state of deficient vascularization, respective conditioned cells secret a mixture of signaling factors with chemotactic and proangiogenic potential that are able to attract bone marrow stromal cells (BM-MSC), as well as to stimulate pre-vascular tube formation and is even more potent than purified, single (recombinant) proteins [36,37]. The great potential of HCM for in situ tissue engineering approaches was already successfully demonstrated in vitro: when integrated as a central depot into scaffolds of biomimetically mineralized collagen, the gradual release of the factors induced migration of BM-MSC and sprouting of endothelial pre-vascular structures into the scaffolds [37].

Consequently, the aim of the present study was to create a cell-free, functionalized bone replacement material system based on the two hypotheses that the incorporation of MBG particles into the CPC matrix/paste leads to an improved degradation of the implant in vivo and that the functionalization of MBG with HCM promotes and accelerates bone regeneration.

2. Materials and methods

2.1. Material and sample preparation

2.1.1. Synthesis of bioactive glass

To synthesize calcium-modified MBG (gCa, molar ratio of Si/Ca/P = 80:15:5) a template-induced, self-assembling sol-gel method based on the protocol developed by Yan et al. [38] was used. In short, the sol was prepared by dissolving 4.0 g of Pluronic P123, a non-ionic block copolymer (molecular weight MW = 5800, Sigma-Aldrich, Steinheim, Germany), in 60 g ethanol (96%) and stirring at room temperature (RT) for 1 h. Following this, 1.0 g of 0.5 M HCl, 6.7 g of tetraethyl orthosilicate (99%, Sigma-Aldrich, Steinheim, Germany, article number: 86578), 0.73 g of triethyl phosphate (99.8%, Sigma-Aldrich, St. Louis, MO, USA, article number: 538728) and 1.4 g of calcium nitrate-tetrahydrate (Merck, Darmstadt, Germany, article number: 1.02121) dissolved in 6 ml deionized water were added. The complete sol was stirred at RT for 24 h. The solution was then transferred into petri dishes and left to dry at RT for 24 h to undergo an evaporation-induced self-assembly process. The obtained gel was dried at 60 °C for 3 h, followed by grinding and calcination at 700 °C for 7 h under air atmosphere. The glass particles were then again grinded and sieved using a 45 μm sieve.

2.1.2. Generation of rat hypoxia conditioned medium (HCM)

Rat bone marrow-derived mesenchymal stromal cells (BM-MSC) of different donors were cultured in T175 flasks in modified Eagle's Medium alpha modification (α-MEM, Thermo Fisher Scientific, Waltham, MA, USA, article number: 32561–029) containing 15% fetal calf serum (FCS; Sigma Aldrich, St. Louis, MO, USA) and 100 U/ml penicillin and 100 μg/ml streptomycin (Pen/Strep; Thermo Fisher Scientific) under normoxic conditions (21% O_2, 5% CO_2, 37 °C) until the cultures reached about 95% confluence. Subsequently, the cells were rinsed once with phosphate buffered saline solution (PBS, Thermo Fisher Scientific)

before medium was replaced by 10 ml Dulbecco's modified Eagle's Medium (DMEM) without phenol red (Thermo Fisher Scientific, article number: 11880–028). Cultivation of the cells was done at 1% O_2, 5% CO_2 and 37 °C under gentle shaking for additional 5 days. Thereafter, rat HCM was collected, dialyzed against deionized water (dialysis tubes with cut off 3.5 kDa, Scienova, Jena, Germany), sterile filtered (0.22 μm) and stored at −80 °C until further use.

2.1.3. Preparation of protein-laden MBG

Protein-laden MBG powder was prepared as described recently [29]. Briefly, protein solution and MBG were mixed in a ratio of 200 μl per 10 mg. For HCM-laden MBG (gCa[HCM]), frozen HCM was freeze-dried and thereafter reconstituted in PBS to achieve concentrated (50x) HCM with a total protein concentration of 36 μg/ml. For FCS (fetal calf serum)-laden MBG (gCa[FCS_x] with x = 4, 40, 400, 4000, 40000 μg/ml), frozen FCS with a total protein concentration of 40000 μg/ml was freeze-dried and reconstituted with PBS to obtain solutions with different protein concentrations. Respective amounts of MBG powder were added to HCM and FCS solutions and mixed using an overhead shaker (neoLab Rotator, neoLab Migge GmbH, Heidelberg, Germany) for 3 h at 25 rpm at room temperature. The MBG was collected by centrifugation, washed with PBS, frozen at −80 °C and subsequently freeze-dried. The protein-laden MBG was then repeatedly sieved through a 45 μm sieve to remove any agglomerates that may have formed after freeze-drying. All steps were performed under sterile conditions and MBG was γ-sterilised (25 kGy) before loading.

2.1.4. Preparation of plottable pastes and scaffold fabrication

Ready-to-use strontium-modified CPC paste (cSr) and carrier liquid (cl) were obtained from INNOTERE GmbH (Radebeul, Germany). The CPC paste consisted of a solid content of 86 wt% with a corresponding content of 14 wt% carrier liquid. The cement precursors contained 57.3 wt% α-tricalcium phosphate, 24.8 wt% calcium hydrogen phosphate, 14.1 wt% strontium carbonate and 3.8 wt% hydroxyapatite [17]. Inorganic impurities in the solid phase were below 0.02 wt% respectively. 10 mg of dissolved cement precursors resulted in ion concentrations below human blood plasma concentrations (see Table S1). The carrier liquid consisted of 80.4 wt% Miglyol 812, 14.7 wt% Cremophor ELP and 4.9 wt% Amphisol A. To prepare CPC-MBG composites, 16 wt% of (protein-laden) MBG were added, calculated according to the amount of CPC paste. To maintain the extrudability of the composite paste, additional cl was added as described earlier [28,29]. All prepared pastes are shown in Table S2. Scaffolds were produced by 3D plotting using a multichannel 3D plotter (BioScaffolder 3.1, GeSiM mbH, Radeberg, Germany). Scaffolds for ion release, cell seeding, microscopy and *in vivo* experiments were plotted in a cylindrical geometry (radius 1.5 mm and 1.6 mm for *in vivo* experiments, 1.6 mm for all other experiments) consisting of 4 layers with a layer-to-layer orientation of 60°, a layer thickness of 0.13 mm and a strand distance of 0.6 mm using a conical 250 μm needle (Globaco, Rödermark, Germany). Scaffolds for mechanical testing were plotted in cylindrical geometry (radius of 6 mm) consisting of 10 layers with a layer-to-layer orientation of 60°, a layer thickness of 0.3 mm and a strand distance of 1.2 mm using a conical 410 μm needle (Globaco, Rödermark, Germany). Afterwards, plotted scaffolds were incubated at 37 °C in a water-saturated atmosphere (humidity >95%) for 3 days. All scaffolds (except those for mechanical testing) were fabricated under sterile conditions whereby CPC paste, carrier liquid as well as protein free MBG were γ-sterilised (25 kGy) beforehand.

2.2. In vitro characterization

2.2.1. Filament fusion and filament collapse test

cSr paste, cSr-gCa(16) and cSr-gCa(16)[FCS_40] composite pastes were evaluated for their plotting behavior and printing fidelity, as proposed by Ribeiro et al. [39]. Instead of HCM, FCS as a comparable complex protein mix was used with a similar total protein concentration (40 μg/ml diluted with PBS). For filament fusion test (n = 3), each material was plotted in three layers on top of each other with a conical 410 μm needle. Within a layer, the strand-to-strand distance increased by 0.2 mm between the strands. Afterwards, strand distances, strand widths and fused segment lengths were measured in images taken by a Leica M205C stereomicroscope (Leica, Wetzlar, Germany). The fused segment length was divided by the strand width to obtain the shape fidelity ratio, which was assigned to its respective strand distance. Optimal shape fidelity was defined at a ratio of 1. For filament collapse test (n = 3), single strands of each material were plotted with a conical 410 μm needle on a platform with pillars placed at known gap distances (1, 2, 4, 8 and 16 mm). The deflection of the filament was quantified by measuring the angle of deflection at the edge of the deposited strand from images directly taken after extrusion using ImageJ software (version 1.53n, National Institutes of Health, Bethesda, MD, USA).

2.2.2. Mechanical testing

Mechanical properties of plotted and set scaffolds (n = 5) of cSr, cSr-gCa(16) and cSr-gCa(16)[FCS] composites were analyzed by performing an uniaxial compressive test with a speed of 1 mm/min using a Zwick universal testing machine (Z010 equipped with a 10 kN load Zell, ZwickRoell, Ulm, Germany) as in previous studies [10,17,28]. Young's modulus and compressive strength were obtained from the data.

2.2.3. HCM characterization – cytokine array

A proteome profiler array for 79 rat cyto- and chemokines was performed according to the manufacturer's instructions (Proteome Profiler Rat XL Cytokine Array Kit, R&D, Minneapolis, MN, USA). Chemiluminescence signals were detected with a gel documentation system (G:BOX, Syngene, Cambrige, UK) and analyzed semi-quantitatively using ImageJ software (National Institutes of Health, Bethesda, MD, USA).

2.2.4. HCM characterization – chemotaxis assay

The chemoattractive potential of the HCM was tested using 2 transwell migration assay systems (Corning HTS Transwell-96 permeable supports, Sigma Aldrich, St. Louis, MO, USA and ChemoTx Disposable Chemotaxis System, Neuroprobe, Gaithersburg, MD, USA) with pore sizes of 8 μm. Therefore, frozen HCM was freeze-dried and reconstituted/concentrated to 50x in α-MEM which was also used for following dilutions. 2.5×10^4 primary rat BM-MSC were starved in serum-free α-MEM for 48 h. Then cells were seeded in 75 μl (Corning HTS Transwell-96 permeable supports) or 50 μl (ChemoTx Disposable Chemotaxis System) DMEM without phenol red or other supplements into the upper chamber, whereas 150 μl (Corning HTS Transwell-96 permeable supports) or 30 μl (ChemoTx Disposable Chemotaxis System) of differently concentrated HCM (0.05x, 0.1x, 0.5x, 1x, 2x, 5x, 10x) or DMEM with 0% FCS (negative control – Ctrl-) and 30% FCS (positive control – Ctrl+), respectively, were added into the lower chamber as chemoattractant. After 24 h, medium was removed, cells were washed with PBS and non-migrated cells on top of the membrane were removed with a cotton swab. The number of migrated cells (Corning HTS Transwell-96 permeable supports) was determined by measurement of lactate dehydrogenase (LDH) activity. Therefore, cells were lysed by incubation in 1% Triton-X-100/PBS for 1 h following determination of LDH activity using the CytoTox 96 Non-Radioactive Cytotoxicity Assay (Promega, Madison, WI, USA) according to the manufacturer's instructions by measuring the absorbance at 490 nm (Infinite M200 Pro, Tecan, Männedorf, Switzerland). Experiments were performed in duplicates with 3 different rat BM-MSC donors.

To visualize the migrated cells (ChemoTx Disposable Chemotaxis System) they were fixed with 100% methanol for 10 min, stained with 0.5% crystal violet in 25% methanol/deionized H_2O for 10 min and rinsed with H_2O until the H_2O stayed clear. Microscopic analysis was performed using a BZ-9000 microscope (Keyence, Osaka, Japan).

2.2.5. HCM characterization – in vitro angiogenesis assay

6.8×10^3 human BM-MSC were seeded into 96-well plates and cultured for 2 days in α-MEM containing 15% FCS and 1% Pen/Strep. Then, the medium was removed and 1.7×10^3 human umbilical vein endothelial cells (HUVEC) resuspended in co-culture medium were seeded on top of the hBM-MSC monolayer and allowed to adhere for at least 4 h. Angiogenesis co-culture medium consisted of a 1:1 mixture of α-MEM and Endothelial Cell Basal Medium (Promocell, Heidelberg, Germany) containing 10% heat-inactivated FCS, 1% Pen/Strep, 100 nM dexamethasone, 50 μM L-ascorbic acid 2-phosphate and 5 mM β-glycerophosphate (all from Sigma-Aldrich).

For investigating the effect of HCM on angiogenesis, frozen HCM was freeze-dried and reconstituted/concentrated to 50x in co-culture medium which was also used for following dilutions. As a next step, 100 μl of co-culture medium containing different concentrations of HCM (0.05x, 0.1x, 0.5x, 1x, 2x, 5x, 10x) were added to each well of the co-culture. Co-culture medium supplemented with 20 ng/ml rhVEGF$_{165}$ (Peprotech, Rocky Hill, NJ, USA) served as positive (Ctrl+) and co-culture medium without VEGF as negative control (Ctrl−).

After 7 days of co-culture with 1 medium change, the cells were washed with PBS and fixed in 4% neutral buffered formaldehyde (FA; SAV LP GmbH, Flintsbach am Inn, Germany). To visualize the formed prevascular structures, fixed samples were washed 3x with PBS, incubated for 30 min with 3% goat serum to block unspecific binding sites, washed 3x with PBS again and incubated for 1 h with a monoclonal antibody against CD31 (mouse anti-human CD31, DAKO, Carpinteria, CA, USA; 1:200 in PBS). After 3x washing with PBS, ZytoChem Plus HRP One-Step Polymer anti-Mouse/Rabbit/Rat (Zytomed Systems GmbH, Berlin, Germany; ready-to-use) was added for 30 min. Then, the samples were washed 3x with PBS and incubated with DAB (3,3-diaminobenzidine; Zytomed Systems GmbH) for approximately 5–10 min. Widefield microscopy was performed using a BZ-9000 microscope (Keyence).

2.2.6. Ion and VEGF release

Calcium, phosphorous (phosphate), silicon (silicate) and strontium ion as well as VEGF release from plotted scaffolds (n = 6) was studied over 28 days. All samples were incubated in 1 ml release medium (Basal Endothelial Medium (PromoCell, Heidelberg, Germany) + 15% heat-inactivated FCS) in a 24-well plate and stored at 37 °C. The wells were blocked beforehand with a 1% BSA (bovine serum albumin) solution. After 1, 4, 7, 10, 14, 17, 21, 24 and 28 days, supernatants were exchanged completely with fresh release medium and collected supernatants were frozen at −80 °C until ion and VEGF content measurement. Ion concentrations were analyzed using inductively coupled plasma-optical emission spectroscopy (ICP-OES, Plasma Quant PQ 9000 Elite, Analytik Jena, Jena, Germany). Therefore, 500 μl of thawed supernatant was diluted 1:10 and acidified with 2% nitric acid. VEGF concentrations were determined with enzyme-linked immunosorbent assay (ELISA) according to the manufacturer's instructions (Rat VEGF$_{165}$ Standard ABTS ELISA Development Kit, PeproTech, Rocky Hill, NJ, USA). Color development was measured with an ELISA plate reader (infinite M200 PRO, Tecan, Switzerland) at 450 nm with wavelength correction at 620 nm.

2.2.7. Cell seeding and fluorescence microscopy

Plotted and set scaffolds (cSr, cSr-gCa(16) and cSr-gCa(16)[HCM]; n = 3) were placed in a 24-well cell culture plate und equilibrated in 1 ml cell culture medium (α-MEM with 15% FCS and Pen/Strep) for 10 min. Medium was then removed and 80 μl of cell culture medium containing 2×10^4 rat BM-MSC were pipetted on top of each scaffold. After 30 min of incubation, 1 ml of cell culture medium was added. Seeded cells were pre-labeled with DiI cell-labelling solution according to the manufacturer's instructions (Vybrant DiI Cell-Labeling Solution, Thermo Fisher Scientific, Eugene, OR, USA). DiI stained the cell membrane in red. Cell seeded scaffolds were then cultivated for up to 28 days under standard cell culture conditions (humidified atmosphere, 21% O_2, 5% CO_2, 37 °C). Cell culture medium was exchanged every 3–4 days. Starting from day 10 on, cell culture medium was changed to α-MEM with 10% FCS, Pen/Strep and osteogenic supplements (10^{-7} M dexamethasone, 10 mM β-glycerophosphate and 0.05 mM ascorbic acid 2-phosphate). Cell coverage was qualitatively analyzed by Calcein AM staining at day 1, 7, 14, 21, 28. Calcein stained the metabolically active cells in green. Imaging was performed with a fluorescence microscope (Keyence BZ 9000, Osaka, Japan).

2.2.8. Scanning electron microscopy

For microstructure analysis, plotted and set scaffolds (cSr, cSr-gCa (16) and cSr-gCa(16)[HCM]) before and after degradation for 28 days in release medium (see ion release) were sputtered with gold and analyzed using scanning electron microscopy (SEM; PhilipsXL30/ESEM, operated in SEM mode at a voltage of 3 kV (spot size 3) with a field emission gun and an Everhart–Thornley detector for secondary electrons). For cell adhesion analysis, scaffolds after fluorescence microscopy were used. Cells were fixed with 2% glutaraldehyde for 30 min at room temperature. Afterwards, the samples were washed with deionized water and gradually dehydrated in an ethanol gradient series of 10%, 30%, 50%, 70%, 80%, 96% and 100% for 30 min each. Ethanol was then replaced with 100% isopropanol for 30 min which was subsequently exchanged with 25%, 50% and 100% HMDS (hexamethyldisilazane). Excessive HMDS was removed and the scaffolds were air dried overnight under a fume hood. Samples were then sputtered with gold and analyzed using SEM as described above for cell-free scaffolds.

2.3. In vivo characterization

2.3.1. In vivo study – animals and surgical procedure

The animal study was approved by the Commission for Animal Studies at the District Government Dresden, Germany (DD24- 5131/ 354/10). For the study, 48 adult male Lewis rats (Janvier Labs, Le Genest-Saint-Isle, France) with an average body weight of 452 ± 25 g and an age of 6 months were chosen. All animals were accommodated according to the current regulations in a light- and temperature-controlled environment. They had access to water *ad libitum* and were fed with pellets (ssniff-Spezialdiäten GmbH, Soest, Germany). After statistical calculation of the required number of animals per group, all rats were randomly divided into the 3 experimental groups, each consisting of 16 animals: cSr, cSr-gCa(16) and cSr-gCa(16)[HCM]. The rats were anesthetized by intraperitoneal injection of ketamine (100 mg/kg body weight) and xylazine (10 mg/kg body weight) and fixed in a dorsal position. An artificial alveolar bone defect with a diameter of 3.3 mm was created surgically in the anterior maxilla of each animal as described previously [40]. According to the randomized distribution, each rat received one bone graft. After insertion of the bone graft, the flap was repositioned, and wound closure was performed using 5–0 Ethilon suture (Ethicon, Norderstedt, Germany). Postoperatively, the animals received 15 mg/kg body weight amoxicillin trihydrate (Fort Dodge Veterinär GmbH, Würselen, Germany) once and 4 mg/kg body weight carprofen (Rimadyl, Pfizer Deutschland GmbH) every 24 h for 4 days. All drugs were injected subcutaneously. The animals were fed with a soft diet for the first 3 days and, subsequently, received a regular diet. Postoperatively, the animals and their behavior were monitored, and the body weight was measured every 2 weeks. For the *ex vivo* assessment of the bone formation, all rats received intraperitoneal injection of the fluorochrome calcein (30 mg/kg body weight) 3 days prior to sacrifice.

2.3.2. In vivo study – sample analysis

After sacrifice, the cranium of each rat was dissected and fixed in 4% formaldehyde. Micro-CT (Micro-computed tomography) and preparation of the histological samples followed.

2.3.3. Micro-CT

One 2D-micro-CT per rat maxilla was performed *ex vivo* using a VivaCT40 (SCANCO Medical AG, Brüttisellen, Switzerland) with the following adjustments: x-ray energy 70 kVp and 114 mA, integration time 200 ms, voxel size 30 μm and cone beam continuous rotation. A 3D reconstruction of the defect area by Software Script (SCANCO) followed. The fitting accuracy of the scaffolds were characterized descriptively. Scaffold degradation was quantified using Dragonfly software Version 2021.1.0.977 for Windows (Object Research Systems (ORS) Inc, Montreal, Canada, 2020; software available at http://www.theobjects.com/dragonfly). As measured by Dragonfly the density of the scaffold was 20% higher compared to cortical bone; the high radiographic density of the scaffolds is caused by the incorporated strontium [15,17]. Thus, density-based segmentation of the scaffold was done by setting the threshold 14% higher than the cortical bone (see Fig. S1 for a step-by-step visualization). For calculation of the degradation rate the mean volume of the remaining scaffold of each group at 6 weeks was divided by the mean volume of the remaining scaffold at 12 weeks. Gaussian error propagation was accounted by calculating the standard deviation as follows:

$$SD_{degradation\ rate} = \sqrt{\left(\frac{SD_{6w}}{mean_{6w}}\right)^2 + \left(\frac{SD_{12w}}{mean_{12w}}\right)^2}$$

2.3.4. Histology

After dehydration in a graded series of ethanol, all samples were embedded in methylmethacrylate (Technovit 9100, HeraeusKulzer, Wehrheim, Germany) as described previously [41]. Coronal sections were produced according to Donath's sawing and grinding technique [42]. Thus, 2–4 central sections of each specimen could be achieved for evaluation. Subsequently, the sections measuring 80–100 μm in thickness were polished. The fluorochrome marker uptake analysis was followed by Masson-Goldner trichrome staining.

2.3.5. Histological analysis

All samples were imaged by fluorescence microscopy and, after staining, by light microscopy (Olympus BX 61, Olympus Deutschland GmbH, Hamburg, Germany) using cell⌂F Imaging Software for Life Science (Olympus). Multiple image alignment was performed using an automatic scanning table (Märzhäuser, Wetzlar, Germany). Thus, 2 to 8 images per sample were scanned with 4×10 and 10×10-fold magnification and manually fused to one image. Fluorochrome marker uptake was analyzed and thereafter all specimens were stained according to Masson-Goldner trichrome staining. A descriptive analysis evaluated the position of the scaffold, the interactions between host bone and bone graft and the bone formation on the defect margins. Again, a 4×10 and 10×10-fold magnification were chosen, and details were enlarged applying a 20×10-fold magnification. For quantification of the osseous healing the following parameter were measured as described previously [12]: remaining defect width related to the particular initial defect width, percentage of the new formed bone related to the particular initial defect area and shortest final distance between scaffold and defect margin. The parameter remaining and initial defect width as well as the shortest initial distance between scaffold and defect margin were quantified, too (see supporting information). All measurements were performed by a blinded examiner.

2.4. Statistical methods

Statistical analysis was performed using GraphPad Prism 9.3.0 (345) (GraphPad Software, La Jolla, CA, United States). Mean and standard deviations were calculated for all groups in terms of a descriptive statistics. Normal distribution was tested. For biomechanical results, a one-way ANOVA with Tukey's multiple comparisons and for ion release a two-way ANOVA with Tukey's multiple comparisons test was applied.

For the migration/chemotaxis assay, a one-way ANOVA with Dunnett's multiple comparisons test was applied to evaluate the differences between the varying HCM concentrations. For the *in vivo* results, a one-way ANOVA with Tukey's multiple comparisons test was applied to evaluate the differences between the experimental groups and within the different healing times. For all analyses the level of significance was set at 95% ($p \leq 0.05$).

3. Results

3.1. Study design

The following schema (Fig. 1) gives an overview over the study design. Strontium-modified CPC paste (cSr), a CPC-MBG composite with 16 wt% addition of MBG (cSr-gCa(16)) and a CPC-MBG composite with HCM-laden MBG (cSr-gCa(16)[HCM]) were used to fabricate 3D plotted scaffolds for *in vitro* degradation and cell seeding experiments, as well as for the implantation *in vivo*. All scaffolds for these experiments came from the same batch. The degradation *in vitro* was analyzed in terms of ion release and the cellular response via qualitative analysis of cell adhesion and proliferation of rat bone marrow stromal cells (BM-MSC). Further, the influence of a complex protein mixture on printing behavior and mechanical properties has been studied and to cover a broad range of total protein concentration (x in μg/ml) for MBG functionalization, FCS (fetal calf serum) as a comparable complex protein mix was used for these experiments (cSr-gCa(16)[FCS_x]). In particular for shape fidelity tests, a FCS concentration similar to the total protein concentration of the generated HCM was used (cSr-gCa(16)[FCS_40]). To complete the *in vitro* part, the generated HCM was characterized to determine the most abundant bioactive factors in the mixture and the functionality of the HCM was tested in terms of cell attractive and angiogenic potential. For the *in vivo* study a rat alveolar cleft model was chosen and 6 and 12 weeks after implantation the degradation and formation of new bone tissue was analyzed via micro-CT and histology.

3.2. In vitro characterization

3.2.1. Printing fidelity and mechanical testing

The printing fidelity of the cSr, cSr-gCa(16) and cSr-gCa(16)[FCS_40] was evaluated by plotting meandering structures with continuously increasing strand distances (Fig. 2A and B). All three materials demonstrated a good printing fidelity and converged quickly to the theoretical optimum. Surprisingly, a tendency of strand fusion for small strand distances was observed for the FCS-free composite cSr-gCa(16) which was not visible anymore for the FCS-containing composite. Additionally, strands of all three materials were plotted over a structure with increasing gaps to analyze the strand stability before post-processing (Fig. 2A, C). With increasing gap width, the deflection angle decreased for all three materials. With the exception of the first gap, where all materials showed a near perfect 90° deflection angle, the FCS-free composite had significant smaller deflection angles for all following gaps and was not able to bridge the last gap as the strand collapsed. Interestingly, the FCS-containing composite showed no such behavior as it could bridge the last gap and no significant difference compared to the pure cement was observed.

Mechanical properties were analyzed for plotted and set, macroporous scaffolds. The addition of MBG significantly decreased the Young's modulus (Fig. 2D) (28 ± 15 MPa) compared to the pure cement (51 ± 18 MPa). Starting with the lowest FCS concentration cSr-gCa(16)[FCS_4] the modulus was even further decreased, but with increasing FCS concentration the modulus increased as well until a similar value, compared to cSr, was reached for the cSr-gCa(16)[FCS_400] group. With increasing FCS concentrations, the Young's modulus decreased again and was significantly lower than the pure cement. Remarkably, all FCS-containing groups showed considerable less deviation compared to the FCS-free groups. For the compressive strength (Fig. 2E) a similar
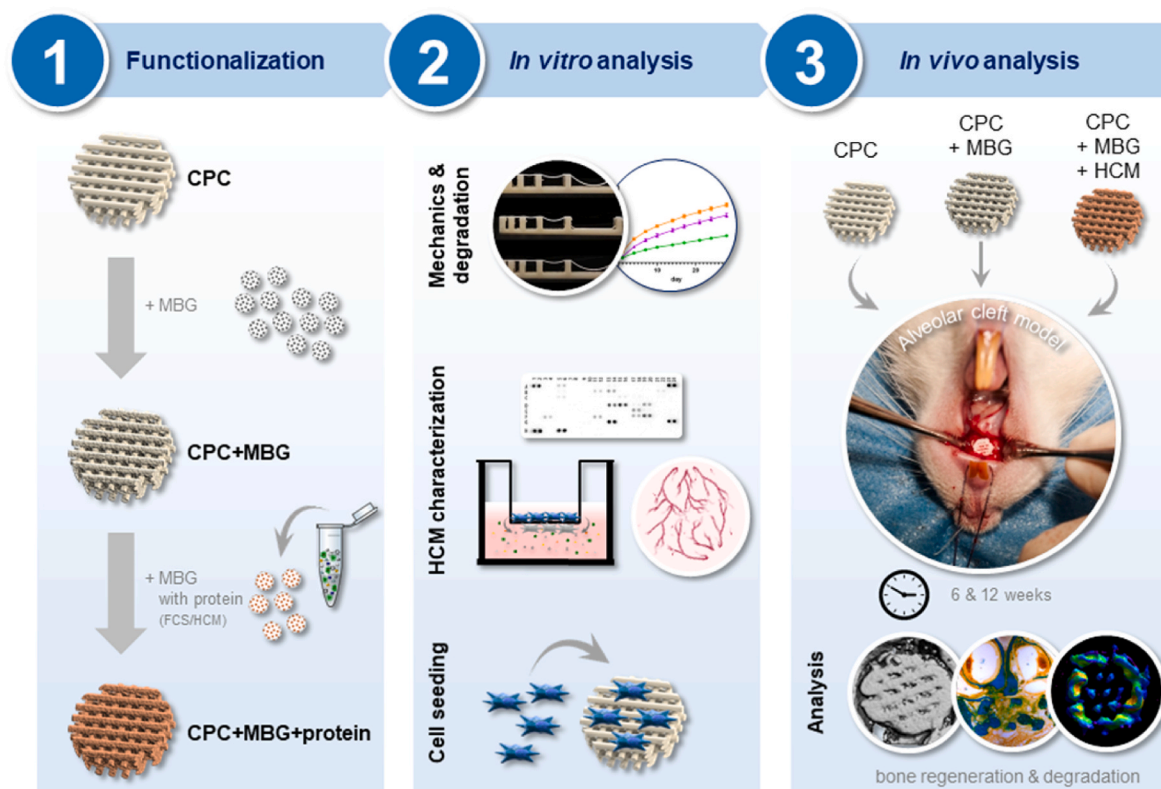
Fig. 1. Schematic overview of the study. Used material groups, analyzed parameters *in vitro* and *in vivo*.

behavior was observed. It was significantly decreased for cSr-gCa(16) [FCS_4] and increased with higher FCS concentrations until cSr-gCa (16)[FCS_400], which even showed a significantly higher compressive strength (3.5 ± 0.1 MPa) than the FCS-free composite (2.0 ± 1.2 MPa). With further FCS concentration increase, the compressive strength decreased, but no significant difference to the FCS-free groups was observed. The deviation for the FCS-containing groups was again considerable smaller compared to the FCS-free groups.

3.2.2. HCM characterization

Specific cyto- and chemokines present in the rat HCM were analyzed using a cytokine array (Fig. 3A, Table S3). Among the 10 most abundant proteins (Fig. 3B), vascular endothelial growth factor (VEGF) was highest followed by Serpin and insulin growth factor binding protein-3 (IGFBP-3).

Rat HCM in different dilutions was also characterized regarding its effect on cell chemotaxis and its ability to induce angiogenesis. Compared to the negative control (medium with 0% fetal calf serum), there was a direct correlation between increasing rat HCM concentration and the number of migrated cells (Fig. 4A and B). Thereby, 5- and 10-fold concentrated rat HCM showed a significantly higher chemoattractive potential towards rat BM-MSC as the negative control.

In contrast to the chemotaxis assay, in the angiogenesis assay more tubular structures were visible when using lower concentrations of rat HCM (Fig. 4C). Tube formation started at a concentration of 0.5x HCM and peaked between 1x and 2x HCM. Although there were still tubes visible when using 5x and 10x HCM, they seemed to be shorter in length.

3.2.3. Ion and VEGF release from plotted scaffolds

The ion release was analyzed from scaffolds incubated in release medium (RM) that had the same geometry as the implants used in the *in vivo* experiment and the same three material groups: Sr-modified cement (cSr), CPC-MBG composite with 16 wt% addition of MBG (cSr-gCa(16)) and CPC-MBG composite with HCM-laden MBG (cSr-gCa(16)[HCM]).

The accumulated release for calcium, phosphorous, silicon and strontium is shown in Fig. 5 (see Fig. S2 for respective release profiles). All three groups showed in total a calcium ion uptake after 28 days of degradation (Fig. 5A). While the pure cement group had a significant higher Ca^{2+} uptake, the MBG-containing groups took up similar amounts of Ca^{2+}. The HCM-loaded composite took up most calcium during the first 10 days, while the HCM-free composite showed a more steady uptake. For phosphorous (Fig. 5B), all three materials showed an initial release (of phosphate ions) that changed at day 4 or day 7 to an uptake and after 28 days there was no significant difference between the groups. Both MBG-containing materials showed an ongoing silicon (silicate ion) release over 28 days (Fig. 5C) indicating a continuous degradation of the glass network. The HCM-free composite although released from day 4 on significantly more silicon than the HCM-containing group. For strontium (Fig. 5D), an ongoing release over the whole period was observed for all three materials. Although the overall strontium content is lower in the composites, both MBG-containing groups released significantly more Sr^{2+} than the pure cement, whereby the HCM-free composite also released significantly more Sr^{2+} than the HCM-loaded group.

The release of VEGF as one key component of HCM was measured from the same scaffolds that were analyzed regarding ion release. However, none of the HCM-containing scaffolds released a clearly detectable VEGF concentration (data not shown). All measured values were well below the first concentration of the calibration line (125 pg ml-1).

3.2.4. Fluorescence and scanning electron microscopy of cell seeded scaffolds

For analysis of cell adhesion and proliferation, rat BM-MSC were seeded on plotted scaffolds of cSr, cSr-gCa(16) and cSr-gCa(16)[HCM] and cultivated for 28 days. In Fig. 6 representative fluorescence images (red channel: pre-labeled cells; green channel: metabolically active living cells) for all three materials at day 1, day 14 and day 28 are
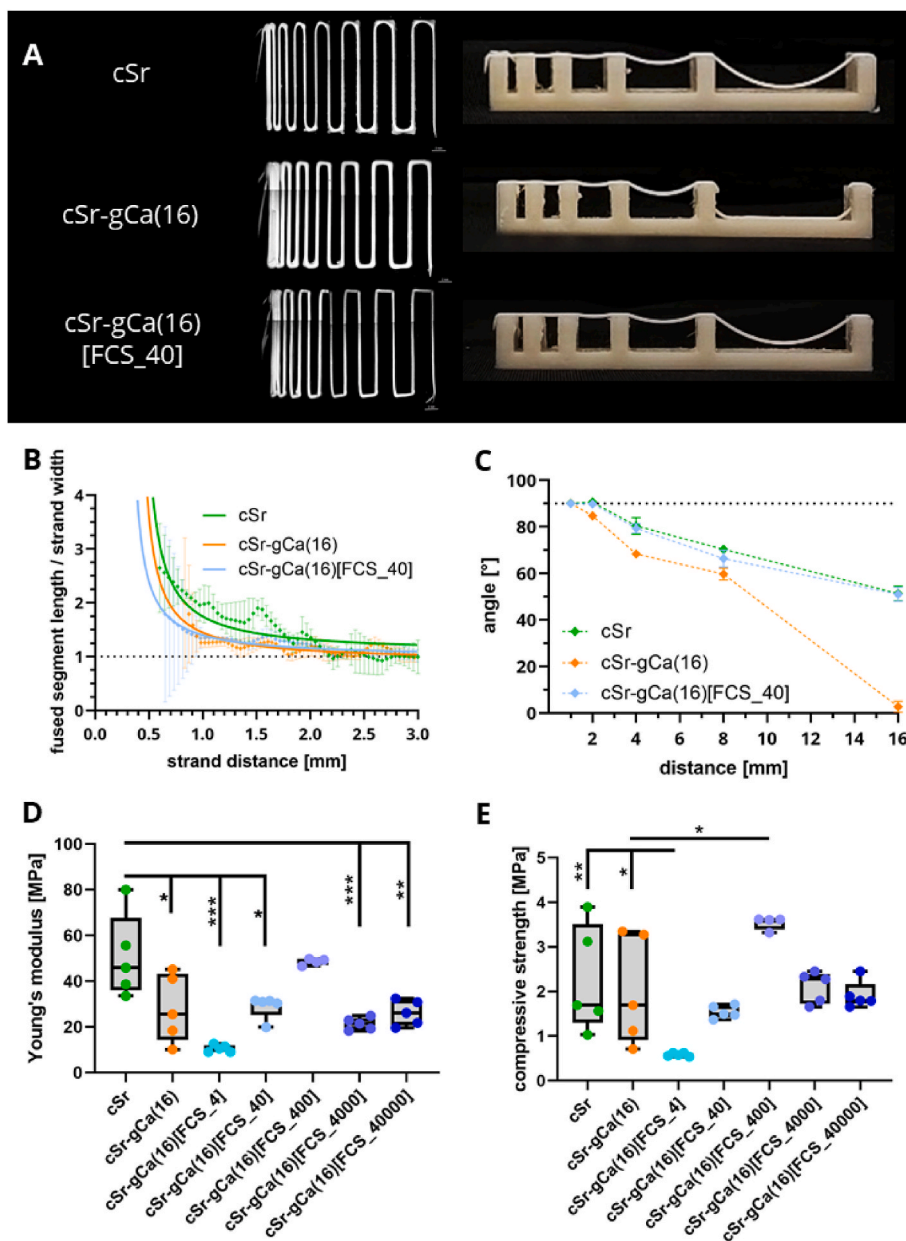
Fig. 2. Printing fidelity and mechanical properties. Representative images of filament fusion and filament collapse test (**A**), quantitative analysis of filament fusion (**B**) and filament collapse (**C**) for Sr-modified cement (cSr), CPC-MBG composite based on cSr with addition of 16 wt% MBG (cSr-gCa(16) and CPC-MBG composite with 16 wt% FCS-laden MBG and a FCS loading concentration of 40 μg/ml (cSr-gCa(16)[FCS_40]; Young's modulus (**D**) and compressive strength (**E**) of plotted and set scaffolds made of cSr, cSr-gCa(16) and CPC-MBG composite with FCS-laden MBG (cSr-gCa(16)[FCS_x] with x = 4, 40, 400, 4000, 40000 μg/ml FCS] (n = 5, box plot with all points min. to max., *p < 0.05, **p < 0.01, ***p < 0.001).

shown. Cells adhered and proliferated on all three scaffold materials over the whole period. While at day 1 mostly single cells were visible (Fig. 6A–C), at day 14 a larger cell network formed on the scaffolds (Fig. 6D–F). A tendency of more cell coverage and larger cell clusters was visible for the HCM-containing scaffolds and the cell network nicely followed the single scaffold strands and apparently span around the cylindrical structures. In contrast the pure cement scaffold showed less cells and a less pronounced cell network. At day 28, even larger cell clusters were observed on the scaffolds (Fig. 6G–I), but only for the HCM-containing scaffolds almost the complete surface of the scaffold is covered with cells, while the cement and the HCM-free composite still had some nearly uncovered areas. In the SEM (scanning electron microscopy) images (Fig. S3) at all time points adherent cells were visible. The spread out cell patches were clearly visible on top of the characteristic hydroxyapatite crystal structure (see Fig. S4 for cell free scaffolds). No distinct differences in cell morphology were visible between the material groups. But starting at day 14 for the HCM-containing group (Fig. S3F) and present for all three materials at day 28, small sphere-like crystal structures were observed (Fig. S3G-I). Interestingly,

the rMSC began to cover them and apparently bridged the space between these spheres.

3.3. In vivo characterization

3.3.1. In vivo results

The *in vivo* analysis was performed in an alveolar cleft rat model (n = 48) evaluating 3 experimental groups cSr, cSr-gCa(16) and cSr-gCa(16) [HCM] (n = 16 each) after 6 and 12 weeks of healing. All rats survived the surgical intervention and showed an uneventful healing. The nutrition was undisturbed and after an initial weight loss the rats gained weight during the healing time. One animal of the cSr-gCa(16) 12 weeks group was excluded due to technical reasons and finally 47 of 48 rats could be included into the analysis.

3.3.2. μCT analysis

After 6 weeks, the descriptive analysis showed in all groups an adequate localization of the printed scaffold within the defect (Fig. 7). Rarely a cant or fracture of the scaffold were detected. No full
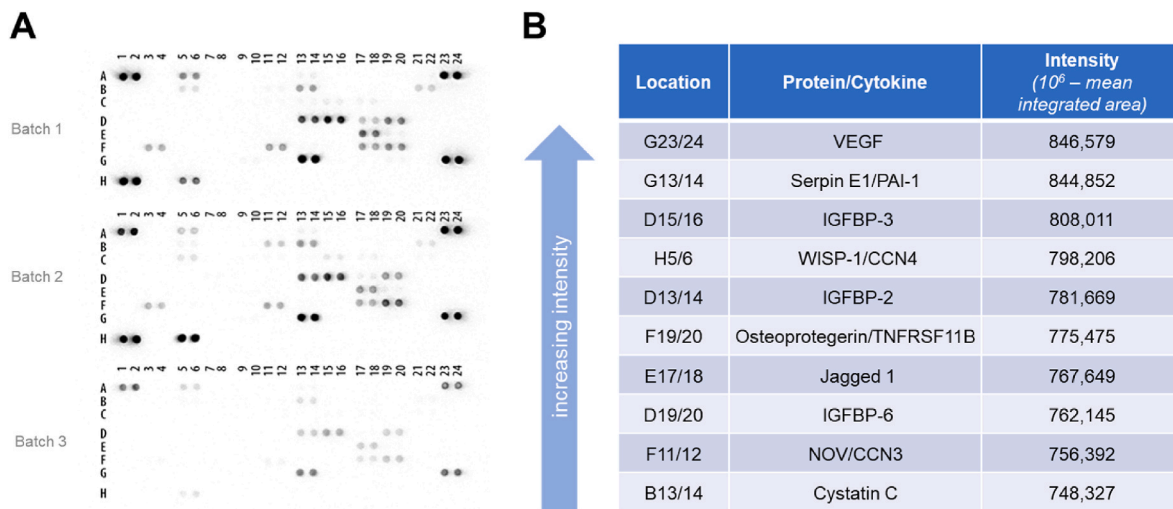
Location	Protein/Cytokine	Intensity (10⁶ – mean integrated area)
G23/24	VEGF	846,579
G13/14	Serpin E1/PAI-1	844,852
D15/16	IGFBP-3	808,011
H5/6	WISP-1/CCN4	798,206
D13/14	IGFBP-2	781,669
F19/20	Osteoprotegerin/TNFRSF11B	775,475
E17/18	Jagged 1	767,649
D19/20	IGFBP-6	762,145
F11/12	NOV/CCN3	756,392
B13/14	Cystatin C	748,327

Fig. 3. Characterization of rat HCM by a rat specific cytokine array. Batch-specific cytokine array profiles (**A**) and mean pixel density of the 10 most abundant proteins/cytokines (**B**) (intensity mean of all 3 analyzed batches).
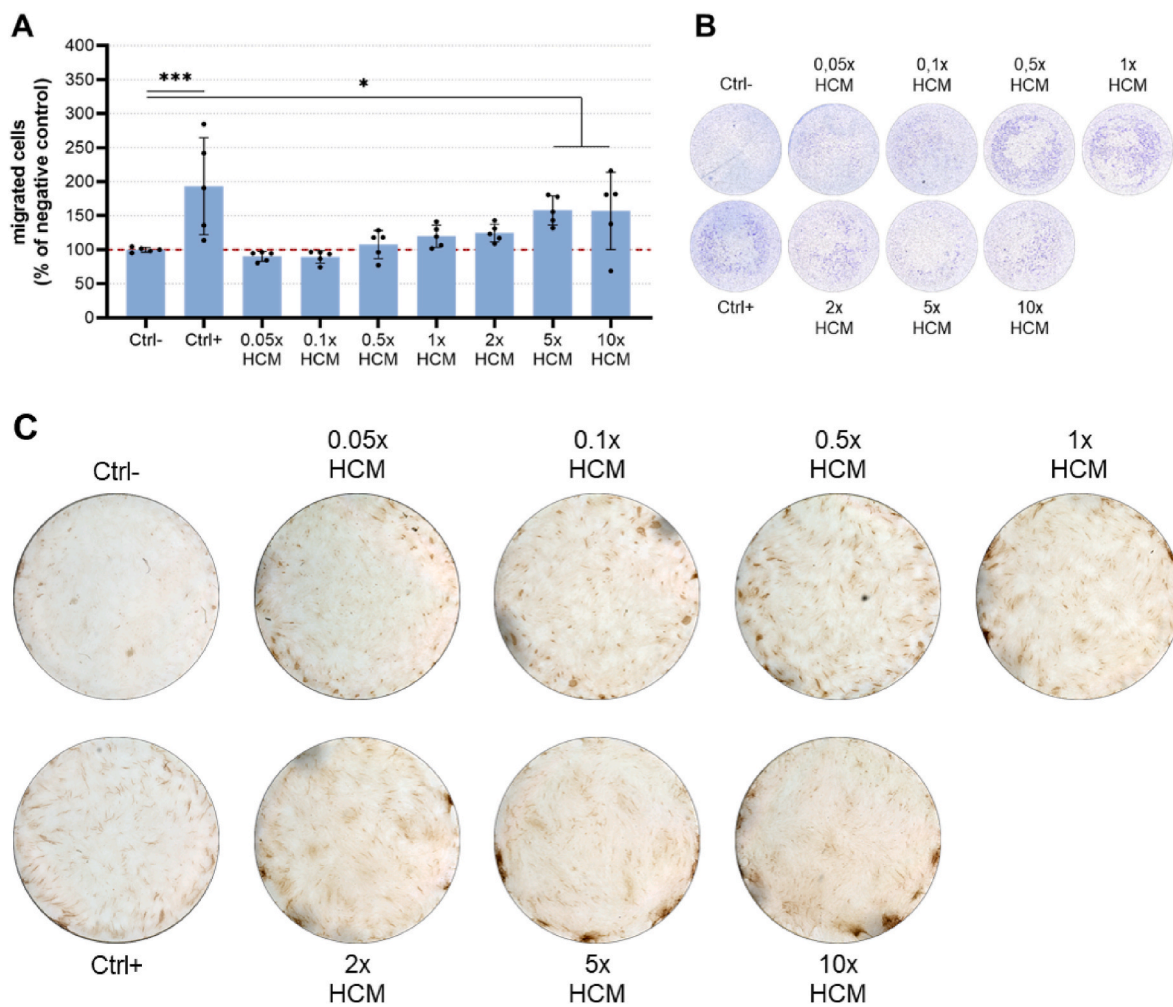
Fig. 4. Transwell migration/chemotaxis and angiogenesis assay. Number of migrated rat BM-MSC towards differently concentrated rat HCM and controls after 24 h incubation as determined by lactate dehydrogenase activity measurement (**A**) (mean ± standard deviation, n = 5, *p < 0.05, ***p < 0.001) and migrated rat BM-MSC after 24 h incubation stained with crystal violet (**B**) (migrated cells = purple, Ctrl-: 0% FCS, Ctrl+: 30% FCS). Angiogenic potential of rat HCM as analyzed by a co-culture of human BM-MSC and human umbilical vein endothelial cells. Typical light microscopic images of tubular structures visualized by CD31 immunostaining after 7 days of cultivation in co-culture medium with different concentrations of rat HCM (**C**) (CD31: dark brown color, Ctrl-: only co-culture medium, Ctrl+: co-culture medium with 20 ng/ml VEGF).
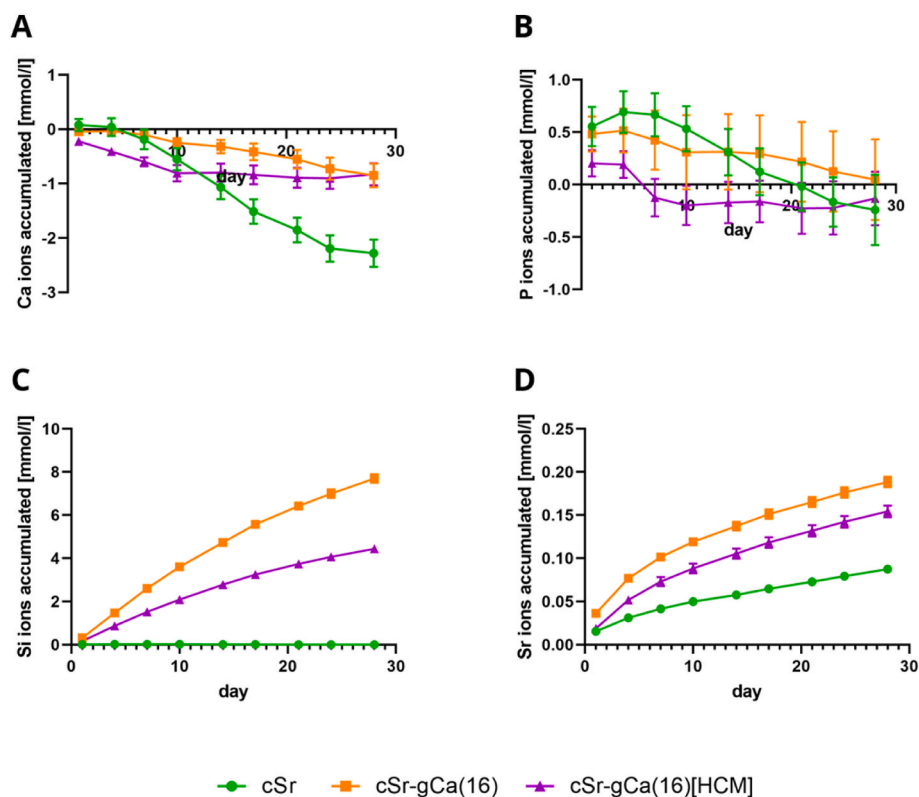
Fig. 5. Accumulated ion release/uptake. Calcium (**A**), phosphorous (**B**), silicon (**C**) and strontium (**D**) release/uptake in RM (release medium) over 28 days from plotted scaffolds made of Sr-modified cement (cSr), CPC-MBG composite based on cSr with 16 wt% addition of MBG (cSr-gCa(16)) and CPC-MBG composite with HCM-laden MBG (cSr-gCa(16)[HCM]). (n = 6, mean ± standard deviation, ion concentration of basal medium is subtracted from measured values - positive slope indicates ion release, negative slope indicates ion uptake from medium).

dislocation of a scaffold out of the defect occurred. The macro design with open pores and dense cement strands was, irrespective of the experimental group, clearly visible (Fig. 7A–C). There was a tendency to thin, newly built bone spiculae at the cranial defect margin for MBG-containing groups. After 12 weeks, the scaffold morphology changed in a way of thinned singular cement strands, which was more pronounced for cSr-gCa(16) and cSr-gCa(16)[HCM] scaffolds as for pure cSr bone grafts (Fig. 7E and F). In some cases, the scaffold appeared as an almost particular material and the initial 60° strand geometry was not obvious anymore after 12 weeks *in vivo*. Anyway, all parts of the biomaterial stayed within the defect area and no dislocation of smaller particles into the surrounding tissues was detectable. The bone formation continued beginning from the defect margin towards the defect center and especially the nose septum (Fig. 7E and F).

Fig. 8 shows the remaining scaffold shape and thickness and scaffold degradation was analyzed by visualization and calculation of the remaining scaffold volume based on µCT data. While 6 weeks after surgery scaffolds were intact and looked quite similar in all groups, after 12 weeks all groups showed clear signs of degradation visualized by a loss of material especially in the scaffold center (Fig. 8A). Compared to cSr, degradation was higher for the MBG-containing scaffolds as seen by less material in the scaffold center and a lower strand thickness. Additionally, the surface of the MBG-containing scaffolds was rougher, which was even significant after 6 weeks for cSr-gCa(16) vs. cSr (Fig. S5).

A quantitative analysis of the degradation revealed that the scaffold volume was comparable among all 3 groups 6 weeks after surgery (Fig. 8B). Although not significant, after 12 weeks mean volumes of MBG-containing scaffolds were much lower as compared to cSr (cSr: 3.07 ± 2.29 mm^3, cSr-gCa(16): 1.39 ± 0.62 mm^3, cSr-gCa(16)[HCM]: 1.38 ± 1.04 mm^3). Thus, the degradation rate was significantly higher when MBG was added to the scaffolds (cSr: 1.23 ± 0.81, cSr-gCa(16): 3.37 ± 0.52, cSr-gCa(16)[HCM]: 2.39 ± 0.84) (Fig. 8C). Interestingly, there was also a significant difference in the mean degradation rate between cSr-gCa(16) and cSr-gCa(16)[HCM].

3.3.3. Histomorphology

3.3.3.1. cSr scaffolds.
After 6 weeks, the fluorochrome labelling showed for all cSr scaffolds an active bone formation at the defect margins and the Masson-Goldner trichrome staining revealed an osteogenesis in terms of cancellous bone formation. Besides the margin area, Calcein marker uptake took place at the maxillary periosteum and all cSr scaffolds exposed a light green autofluorescence. Between the scaffolds themselves and the defect margins were gaps in varying dimensions, which were bridged by soft tissue (Fig. S6A). The layer architecture of the scaffolds with round shaped strands was still present and the areas between the macropores were filled with soft tissue (Fig. 9A).

After 12 weeks, the Calcein labelling was comparably reduced. No complete osseous healing of the defect was observed, but the bone formation at the margins continued and had a cone like structure with more lamellar bone at the interface to the initial defect margin and a cancellous bone structure towards the center (Fig. 9D). The nasal mucosa cranial to the defect was predominantly (approx. 75% of the cases) regenerated and a close contact to the scaffold did not affect this process. Most parts of the cSr scaffolds were still embedded in soft tissue, but a guiding function of the cement for the newly formed bone was clearly detectable (Fig. S6B). Further, there was no morphological difference between the soft tissue within the defect and the regular present oral soft tissue adjacent to the artificial defect. Regarding the morphology of the bone grafts, their surface appeared mostly still smooth and the layer architecture persisted.

3.3.3.2. cSr-gCa(16) scaffolds.
For scaffolds of this experimental group, the Calcein labelling was comparable to the previous group. After 6 weeks, the Masson-Goldner trichrome staining showed a tendency to thicker, newly formed, cone-like bone spiculae growing towards the defect center compared to pure cSr grafts (Fig. 9B). If there was a close initial contact between cSr-gCa(16) scaffolds and host bone, an osseous integration or osseous growth along the biomaterial surface occurred, but a complete osseous bridging of the defect was not observed
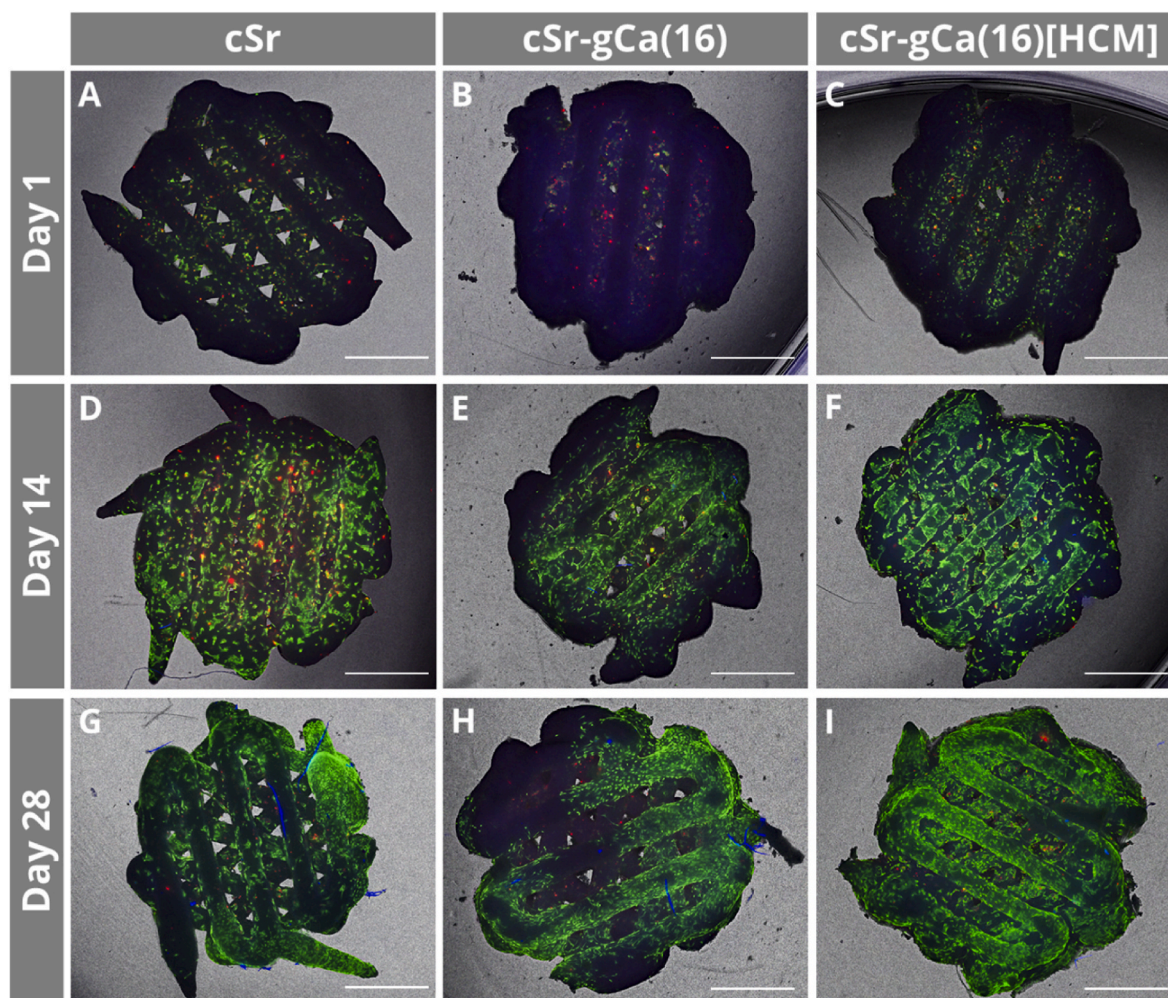
Fig. 6. Fluorescence images of rMSC seeded on plotted scaffolds. DiI pre-labeled (red channel) and calcein stained (green channel) (blue: autofluorescence) rMSC seeded on top of plotted scaffolds made of Sr-modified cement (**A,D,G**), CPC-MBG composite based on cSr with 16 wt% addition of MBG (**B,E,H**) and CPC-MBG composite with HCM-laden MBG (**C,F,I**) at day 1 (upper row) at day 14 (middle row) and at day 28 (lower row) (scale bars = 1 mm).

(Fig. S6C). After 12 weeks, more specimen with a partial osseous integration of the biomaterial could be detected compared to after 6 weeks. This is also remarkable in comparison to the cSr group where no osseous integrations were visible. Overall, there was an ongoing bone formation for the cSr-gCa(16) group based on the findings of the ongoing fluorescence marker uptake and presence of cancellous bone (Fig. 9E, Fig. S6D). During the healing time the scaffold surface appeared to be getting noticeably rougher and the cement strands less rounded indicating material degradation. This was more pronounced for this experimental group compared to the cSr bone grafts.

3.3.3.3. cSr-gCa(16)[HCM] scaffolds. After 6 weeks, osteogenesis within the defect region was advanced compared to the other groups, visible in both fluorochome labelling and Masson-Goldner trichrome staining. In one case new bone, starting from the nasal site, has grown through the entire scaffold, but in the other cases, the defect was still open at this time point. As in the other groups, the scaffolds were located in the defect area, but with a tendency towards more material dislocation. Regarding the scaffold structure, smooth as well as rough surface areas could be identified (Fig. 9C). This represents a morphological difference to pure cSr scaffolds, which were characterized by an almost smooth and rounded surface after 6 weeks. After 12 weeks, in this experimental group seven unilateral and two bilateral osseous defect bridging occurred, which indicates a pronounced and ongoing bone formation. The defect bridging took place in all cases at the cranial

defect site and the scaffold acted as a guiding structure. The nasal mucosa was also fully recovered in these areas of osseous bridging (Fig. 9F, J). The scaffolds were still present at the end of the study, but their shape was now increasingly irregular indicating resorption at the surface (Fig. 9F). Compared to pure cSr and cSr-gCa(16) scaffolds, the degradation of cSr-gCa(16)[HCM] bone grafts was more pronounced after 12 weeks.

3.3.4. Histomorphometry

After 6 weeks, the percentage of remaining defect width in relation to the individual initial defect width were 86.9 ± 5.8% for cSr group (mean ± SD), 83.6 ± 6.9% for cSr-gCa(16) and 80.2 ± 8.8% for cSr-gCa(16)[HCM] scaffolds. With ongoing healing time the following values for the remaining defect width were measured: 86.2 ± 7.3% for cSr, 85.1 ± 7.1% for cSr-gCa(16) and 65.6 ± 19.4% for cSr-gCa(16)[HCM] bone grafts. The HCM containing scaffolds exposed statistically significantly smaller defects compared to the other two groups after 12 weeks (Fig. 10A).

Bone formation was also determined in relation to the individual initial defect area. After 6 weeks, cSr Scaffolds led to a bone formation rate of 6.3 ± 2.6% after 6 weeks, whereas the cSr-gCa(16) group showed 9.1 ± 2.7% and the cSr-gCa(16)[HCM] group 10.3 ± 5.8%. After 12 weeks for all groups increased bone formation values could be measured: 9.5 ± 5.1% for cSr group, 11.4 ± 6.7% for cSr-gCa(16) and 17.7 ± 8.5% for cSr-gCa(16)[HCM] scaffolds, whereas the increase was
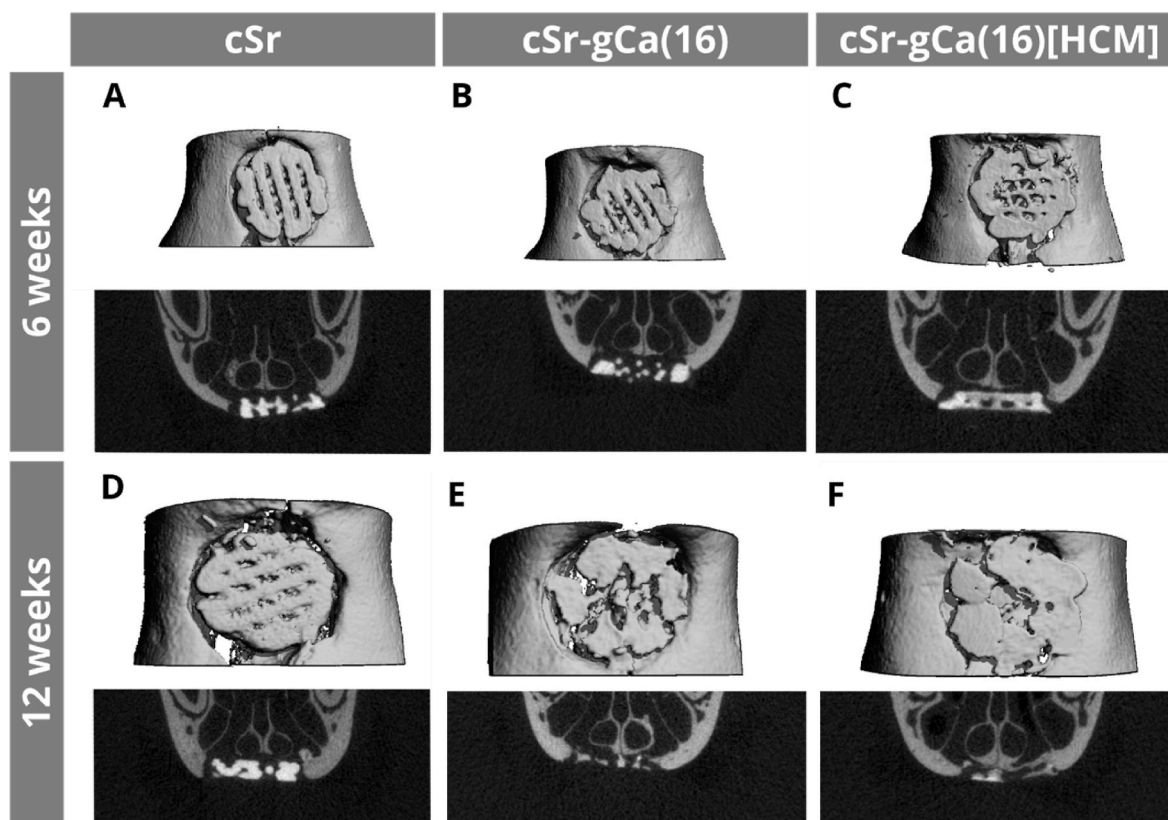
Fig. 7. Micro-CT of a grafted bone defect in a rat maxilla. 3D reconstruction (white background) and coronal sections (black background) of representative images after 6 (**A, B, C**) and 12 weeks (**D, E, F**) of healing.

not found to be statistically significant and the scaffolds containing HCM showed the highest increase of within the healing time (Fig. 10B).

Initially, at the time point of insertion, all scaffolds exposed almost the same position within the artificially created bone defect and there were no statistically significant differences regarding the initial distance between scaffold and defect margin measurable. However, in all groups the distance decreased comparing the initial and final values at the end of the study. The final distance revealed differences between the groups. After 6 weeks, the final distances between scaffold and defect margin were 109 ± 60 μm for cSr, 54 ± 36 μm for cSr-gCa(16) and 86 ± 58 μm for cSr-gCa(16)[HCM] scaffolds. After 12 weeks the development of this parameter varied and the cSr-gCa(16)[HCM] scaffolds displayed a significant shorter final distance between scaffold and defect margin of 33 ± 26 μm compared to cSr group (Fig. 10C).

The values for the initial and remaining defect width as well as the initial distance scaffold-defect margin are included into the supporting information (Table S4, Table S5, Fig. S7).

4. Discussion

CaP materials are outstanding bone substitutes and widely accepted in orthopedic and maxillofacial surgery. Hence, for the treatment of large osseous defects, injectable CPC formulations were developed for an easy clinical application. The adaption of these formulation for 3D plotting opens up the possibility for fabrication of larger and macroporous, as well as defect- and therefore patient-specific implants. However, for the application of extrusion-based additive manufacturing the materials used need to fulfill some requirements, as they have to be extrudable and remain a certain shape fidelity after extrusion. Rheological analysis of the cl-based CPC and CPC-MBG composite pastes revealed the desired shear thinning behavior in previous studies [17, 29]. Besides the viscosity, the filament fusion and filament collapse test

proposed by Ribeiro et al. are suitable methods to assess the printing fidelity of newly developed materials for extrusion-based 3D printing [39]. All three materials used in this study showed good printingfidelity, although a tendency of strand fusion for small strand distances was observed for protein-free composite cSr-gCa(16). A possible explanation could be the additional carrier liquid added to the composite to compensate the higher solid content by the addition of MBG powder. The interaction between carrier liquid and glass powder could be different compared to the cement precursors. A similar behavior was seen in our recent study: The increase of glass content in the composite, and therefore also increased amount of cl, led to a trend of decreasing viscosity [29]. Interestingly, the addition of the protein mixture seems to counteract this, as the protein-containing composite (cSr-gCa(16) [FCS_40]) converged the fastest to the theoretical optimum. This stabilizing effect during plotting was even more obvious in the filament collapse test, as the protein-free composite was not able to bridge the largest gap, in contrast to the FCS-containing composite. Rheological analysis showed that all prepared pastes had a shear thinning behavior (see Fig. S8) and for all MBG-containing groups the viscosity was decreased, probably due to the mentioned additional amount of carrier liquid needed. The incorporation of FCS increased the viscosity again, however no clear trend for different FCS concentrations was observed.

Besides these printing parameters, mechanical properties of fabricated constructs can be crucial, as implants in bone defects usually experience mechanical loads. The influence of incorporated MBG particles on compressive strength and Young's modulus of the composites has been analyzed before. For example Schumacher et al. showed for freshly fabricated and set bulk samples based on a p/l-CPC that there is no difference between pure CPC and CPC-MBG scaffolds in terms of compressive strength, while Li et al. saw a tendency to a decreased compressive strength and modulus for their printed p/l-CPC-MBG constructs [27,43]. In the present study, we observed a significant decrease
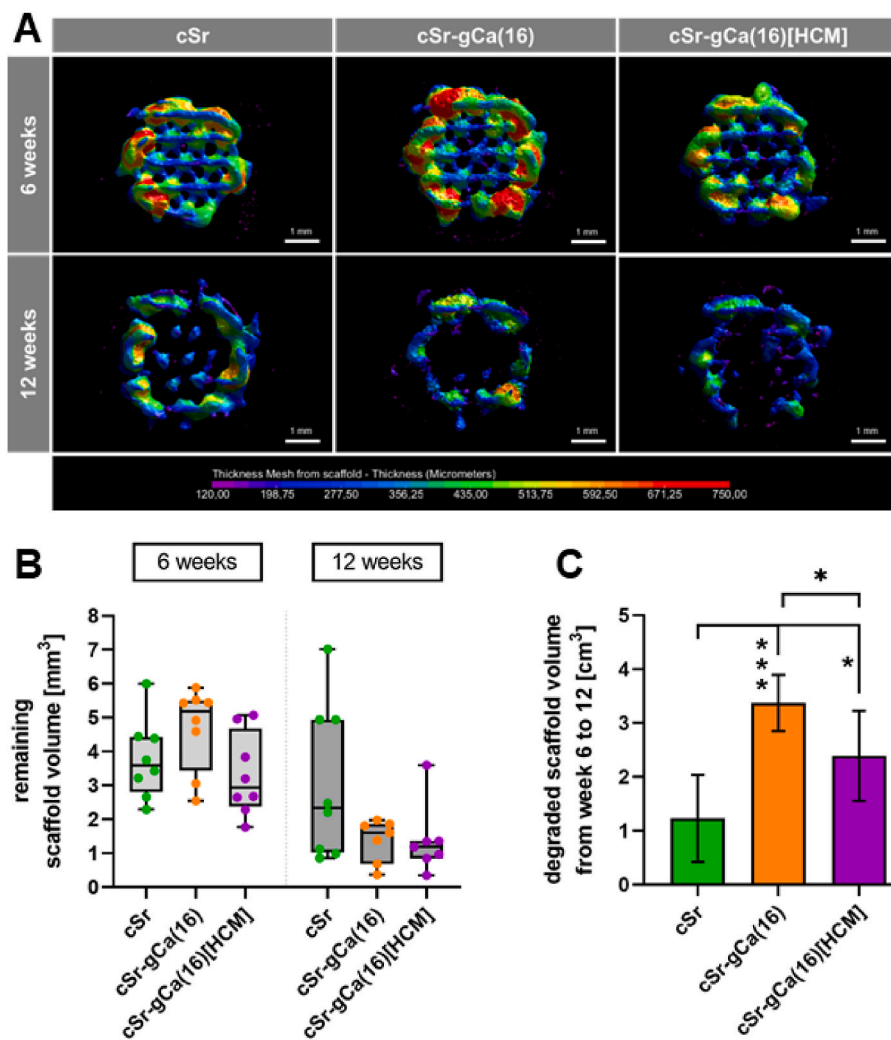
Fig. 8. In vivo scaffold degradation analyzed by μCT. Remaining scaffold shape and thickness 6 and 12 weeks after surgery as evaluated by μCT measurement (**A**) (thickness range: 120–750 μm, violet – red; scale bar = 1 mm). Scaffold degradation described by the remaining scaffold volume 6 and 12 weeks after surgery as evaluated by μCT measurement (**B**) (n = 8, box plot with all points min. to max., *p < 0.05) and the calculated degradation rate (**C**) (mean ± standard deviation, *p < 0.05, ***p < 0.001).

in the modulus and no change in the compressive strength between the pure cSr and the protein-free composites. Several studies have shown that the incorporation of MBG into CPC does not change the microstructure and formation of nanocrystalline hydroxyapatite and also in the present study no difference to the usually observed microstructure was seen in the SEM images [28,44]. The different results for mechanical properties can therefore probably be attributed to the different CPC to MBG ratios and different scaffold geometries used in the studies. The incorporation of complex protein mixtures and their influence on mechanical properties though has to the best knowledge of the authors, not been studied so far for such a composite. Similar to the printing behavior, the addition of protein showed a stabilizing effect, but only for certain protein concentrations. While for the lowest and highest concentrations no change or even a significant decrease in compressive strength and Young's modulus was observed, a concentration of 400 μg/ml FCS compensated these negative effects of MBG integration or even led to a significant improvement compared to the protein-free composite. Regardless of the protein concentration, the addition of FCS led to a homogenizing effect as all protein containing groups showed considerable less deviation in contrast to the FCS-free groups. The exact mechanism behind this behavior is not yet known and more detailed studies are needed to determine whether this is an FCS-specific or a general protein-based effect. A possible explanation might be that the incorporation of proteins leads to a different interaction between the crystalline CPC phase and the MBG particles. Differences in surface charge could influence the electrostatic bonding between CPC, protein

and MBG and therefore improve or impair the transmission of mechanical loads between these three phases. The importance of the surface charge for the binding properties was nicely shown for proteins and mesoporous silica [45] and this effect will most certainly translate into a CPC-MBG system.

Attraction, mitosis and differentiation of (stem) cells and sufficient nutrient and oxygen supply by a functioning vasculature are key components for tissue regeneration. Thus, using chemoattractive and proangiogenic factors to induce and stimulate these processes seems to be a promising strategy to enhance tissue regeneration. Due to the highly differentiated interplay between cells, combinations of bioactive factors are potentially more efficient than the use of single ones. Instead of using several recombinant growth factors, there are also naturally occurring bioactive factor mixtures available. One of them is hypoxia conditioned medium (HCM) that – since hypoxia mimics the state of deficient vascularization - contains a complex mixture of signaling and proangiogenic factors [37,46–48]. The effectiveness of HCM regarding chemoattraction of cells has been shown for different species as well as for scaffold-based approaches [36,37]. Due to its natural origin, the composition of HCM is batch-dependent and should always be characterized. As analyzed by a chemokine array, the most abundant protein in the rat HCM used in this study is VEGF. VEGF stimulates mitosis, migration and permeability of endothelial cells and has emerged as the single most important regulator of blood vessel formation in health and disease. It has been found in all vertebrates and is highly conserved between species [49]. The homology between human and rat VEGF e. g.
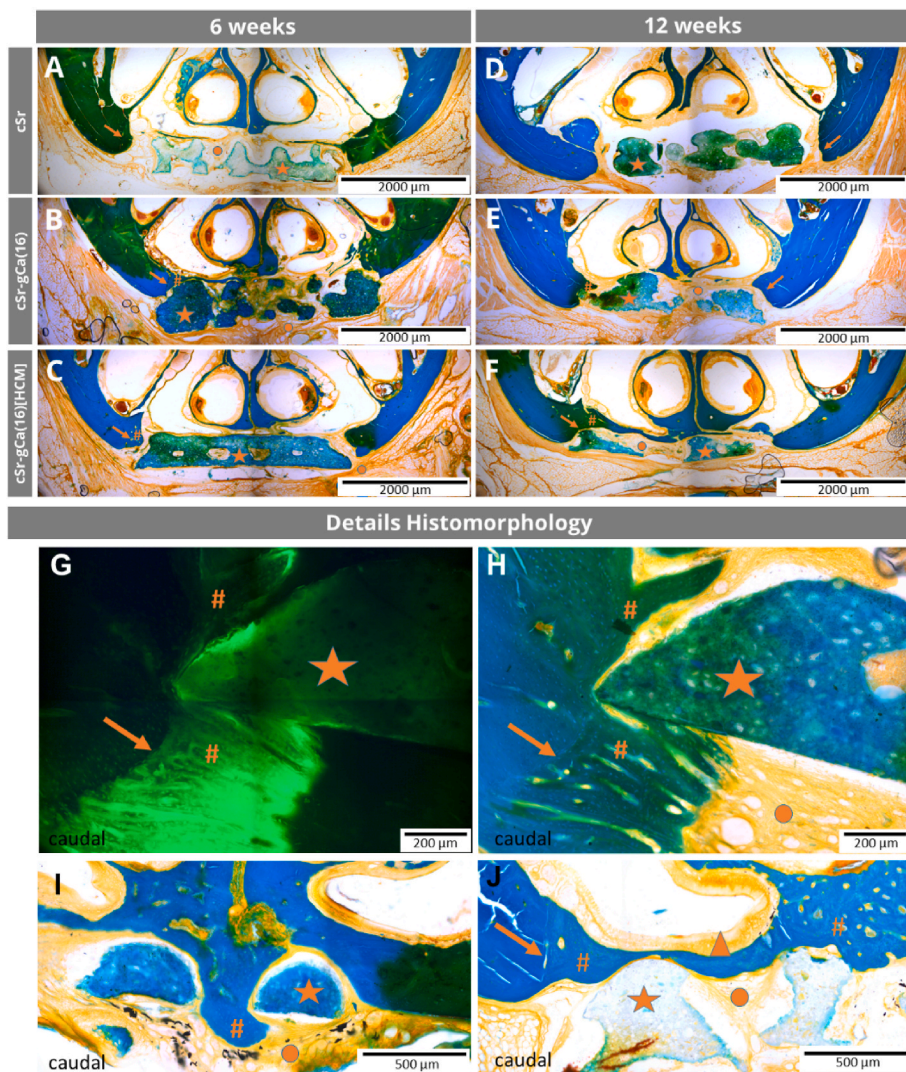
Fig. 9. Histomorphology in rat cleft model. Healing time of 6 (**A-C**) and 12 weeks (**D-F**). In all groups A-F the scaffolds were in the center of the artificial maxillary defect and bone formation started from the defect margins. The extent of the osteogenesis as well as the degradations behavior of the bone grafts varied between the 3 experimental groups and healing times. Histomorphology details of cSr-gCa(16[HCM] group (**G-J**): Close contact between cSr-gCa(16) [HCM] bone graft (★) and new formed bone (#) and soft tissue (●) after 6 (G, H, I) and 12 (J) weeks of healing. The initial margin of the artificial maxillary bone defect is still detectable due to the morphological characteristics of lamellar bone (→). In I, new formed bone went through the entire scaffold and continued at the caudal site of it. The printed bone graft acted as a guiding structure and the previous defect is completely bridged by new formed bone (J). Even the respiratory mucosa of the nasal cavity recovered completely (▲). Masson-Goldner trichrome staining (all except G), Calcein fluorochrome labelling (G), multiple image alignment, coronal sections, scale bar represents 2000 μm (A–F), 200 μm (G, H) and 500 μm (I, J).
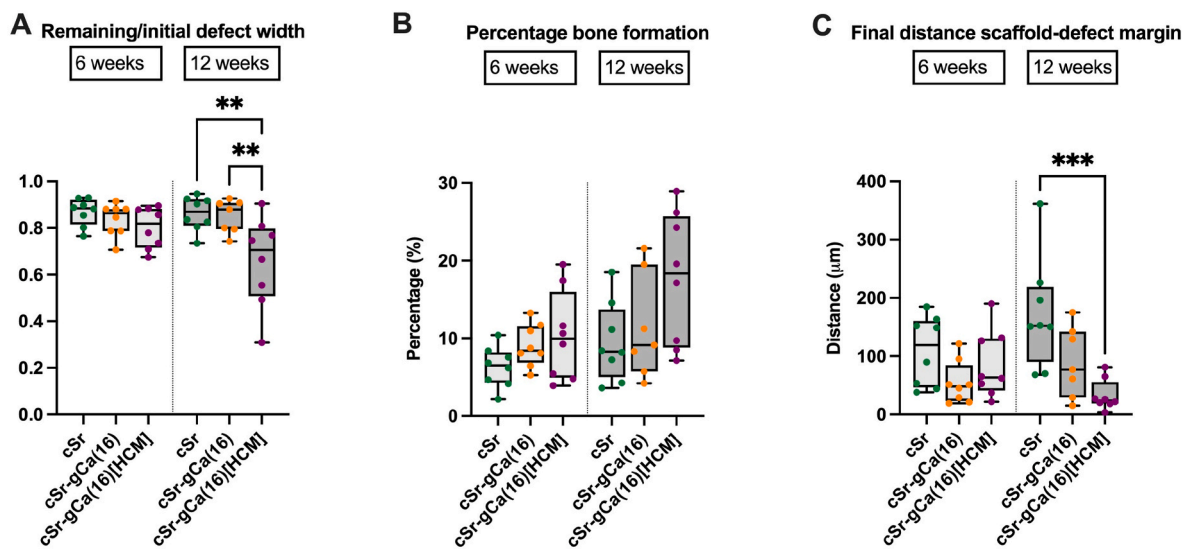
Fig. 10. Histomorphometric analysis of defect healing. Results for the parameter remaining defect width related to the particular initial defect width (**A**), percentage of the new formed bone related to the particular initial defect area (**B**) and shortest final distance between scaffold and defect margin (**C**) for all experimental groups after 6 and 12 weeks of healing (n = 7 or 8; overall animals: 47, box plot with all points min. to max., **p < 0.01, ***p < 0.001).

is 88% and it has been shown that rodent VEGF is active on human cells and vice versa [50]. In the angiogenesis assay performed in this study we were able to show a comparable angiogenic potential of HCM to the positive control (20 ng/ml rhVEGF$_{165}$). Here, tube formation started at a concentration of 0.5x HCM and peaked between 1x and 2x HCM which corresponds to VEGF concentrations in the pg/mL range (1x HCM: 40–80 pg/ml as determined by ELISA, data not shown). Since the VEGF concentration in HCM is about 1000-fold lower than the positive control, it seems obvious that tube formation is mediated by synergistic action of the different bioactive factors present in HCM. Recently, similar effects could also be shown for human HCM [37]. The cellular communication network factor 1 (CCN1) that is also present in HCM in low amounts (Table S3) e. g. is essential for the control of angiogenesis by providing positional information to endothelial cells during the outgrowth and maturation of blood vessel sprouts, fine-controlling notch-dependent, inter-endothelial cell communications and mediating interaction with inflammatory cells [51]. On the other hand, HCM also contains angiogenesis inhibiting factors like IGFBP-6 or Endostatin that might be necessary to keep a physiological balance [52,53]. Migration of BM-MSC in this study was correlated to the HCM concentration showing highest numbers of migrated cells at 5x and 10x HCM. Insulin growth factor binding protein-3 (IGFBP-3), the third most abundant protein present in HCM, is reported to recruit hematopoietic and endothelial precursor cells and restore the function of injured vasculature [54,55]. Recently, Deng et al. showed that IGFBP-3 also stimulates the migration of BM-MSC in a dose-dependent manner [56]. While *in vitro* at 25 ng/ml IGFBP-3 the number of migrated cells was highest, concentrations above 25 ng/ml inhibited cell migration. *In vivo* scaffolds seeded with cells where the IGFBP-3 gene was knocked down, attracted 10-fold less endogenous MSC and in turn led to inferior bone regeneration of a segmental femoral defect. Even though concentrations of the specific factors differ among different species, the overall composition and the chemoattractive and angiogenic potential of HCM is similar [36,47]. In this study, the cell-stimulating effects of rat HCM were proven *in vitro* which helps to explain the enhanced bone regeneration induced by HCM-functionalized MBG-CPC scaffolds *in vivo*. However, it should be noted that for the *in vivo* experiments a higher HCM concentration compared to the optimal concentration observed in the *in vitro* experiments was necessary, because the CPC matrix that is surrounding HCM-functionalized MBG particles blocks the release of HCM components and reduces the effectively released HCM concentration.

One major requirement for bone replacement materials used in (*in situ*) tissue engineering is their biodegradability. As they support the regeneration of damaged tissue or replace missing material, they have to degrade over time to enable growth of new tissue. Additionally, through their degradation biomaterials can deliver desired cell-inducing stimuli. Although CPC is widely used as a bone replacement material, one of key disadvantages is their slow degradation and resorption *in vivo* [12,16, 22]. This is largely attributed to two factors: 1) The CPC set into hydroxyapatite which has a low solubility in physiological conditions and degrades mainly by cellular resorption and 2) CPC is often used as an injectable material system and the resulting bulk scaffolds have a low surface-to-volume ratio and a lack of macroporosity, which is not only essential for degradation, but also for cell ingrowth and supply of oxygen and nutrient of the newly formed tissue. There are different strategies to improve the degradation of CPC for example with fabrication-based methods like foaming of CPC to induce macroporosity [9,57,58]. With the advances of additive manufacturing and the development of processable CPC pastes, 3D plotting of CPC even allows fabrication of scaffolds with a defined macroporosity [8,11,59]. The second strategy is to combine CPC with a faster degrading material. Biodegradable polymers like alginate, gelatin or chitosan are several prominent examples from this large material class that have been used in several studies [14, 59–61]. As an alternative mesoporous bioactive glasses can be incorporated, because due to their intrinsic high porosity they not only

increase the initial porosity of CPC constructs, but also increase the scaffold porosity over time because of their faster degradation [29]. Like polymers, MBG can be combined with CPC to composites that are applicable for 3D plotting and take advantage of both mentioned strategies [28,29,43]. Moreover, through the amount of added MBG, it is possible to adjust the degradation in terms of ion release to a desired level [29].

As also observed in a previous study, the incorporation of MBG led to a significant higher release of strontium ions [29]. As strontium is only present in the CPC matrix, the higher release can be directly attributed to a faster degradation of the CPC due to the combination with MBG. The HCM-free composite released significantly more Sr^{2+} than the HCM-loaded composite which can probably be explained by the difference in MBG degradation in both groups. As silicon is the major component of the glass network, the measurement of released silicon ions is the main indicator for the glass degradation. The HCM-free group showed a significantly higher silicon release compared to the HCM-loaded composite. As the amount and the chemical composition of the glass is the same for both groups, the difference can only be explained by the functionalization with the HCM. It is possible, that the layer of protein on the glass surface impairs the degradation of the glass network as it blocks the formation of silanol groups (Si–OH) in contact with an aqueous environment. According to the most prevalent theory, the formation of silanol groups is the first step in the degradation process of bioglasses [25,62]. With the formation of Si–OH groups the pH value is locally increased and breaks up the Si–O–Si bonds of the class network and leads to even more Si–OH groups. If present in the surrounding solution, Ca^{2+} and PO_4^{3-} will later on migrate to the surface of the glass, forming a CaO–P_2O_5 layer, which will ultimately lead to the crystallization of hydroxyapatite [25,62]. This behavior can be seen for both composites in the ICP data, as both show an uptake of calcium and phosphate ions over time. Especially at earlier time points this uptake is higher for the HCM-loaded group, which could be again explained by the slower glass degradation, as the release of calcium and phosphate ions from the glass network itself is blocked by the protein layer and more ions have to be taken up from the surrounding medium. A similar behavior of calcium and phosphate uptake was observed for the pure CPC, which is a known effect. During setting, the CPC forms a calcium-deficient hydroxyapatite and in contact with calcium and phosphate containing solutions an uptake of both ions is initiated [63].

The degradation behavior observed *in vitro* is mirrored by the degradation *in vivo*. As analyzed by μCT, the degradation rate of MBG-containing CPC scaffolds was significantly higher compared to the pure CPC. Thereby, in line with the *in vitro* results, the degradation rate was highest for HCM-free composites. That could be explained by their enhanced silicone ion release as an indicator for the glass degradation which in turn also led to the enlarged and rough surface area after 6 weeks *in vivo*.

Clinically, the degradation rate is of high relevance for the treatment of alveolar clefts in humans, because the scaffold needs to be replaced by autologous bone tissue during healing, because a tooth has to be transposed into the previous cleft area. This is especially important, if a bone graft is inserted into a growing organism like a child suffering from an alveolar cleft. In the current study, the hypothesis of improved *in vivo* scaffold degradation by incorporation of MBG particles into the cement could be confirmed. For a clinically successful bone graft the osteoinductive and osteoconductive properties are crucial as well and the study showed, that the functionalization of MBG with HCM promotes and accelerates bone regeneration *in vivo*. The *in situ* tissue engineering approach is not the only promising strategy to develop an alternative bone graft for critical size or hereditary alveolar bone defects. Several years tissue engineering was seen as a promising approach and preclinical studies in alveolar cleft models as well as clinical pilot studies were realized [64]. The rat is a commonly applied animal model for testing new biomaterials and in the maxilla a cleft-like bone defect can be created artificially to insert *in vitro* created bone grafts [32,41,65].

The first studies in the same defect model as the current one, evaluated tissue engineered bone grafts containing alloplastic as well as xenogenic scaffold materials which were colonized with undifferentiated or osteogenic differentiated rMSC [40,41]. The results for the nanocrystalline calcium phosphate/silica matrix particle colonized with undifferentiated MSC revealed a significant reduction of the remaining defect volume and width compared to a control or pure scaffolds after 6 weeks of healing, but a relevant issue of this study was the unstable fixation of the particle in the bone defect and a fibrous integration of the dislocated scaffold fraction [41]. The phenomena of particle dislocation was also detectable for initially more stable, fleece-like scaffolds consisting of bovine hydroxyapatite and collagen [40]. In this study rMSC-free scaffolds lead to the smallest remaining defect width and a bone formation, which was superior to the other scaffolds after 12 weeks. There was no advantage of a pre-insertion cell colonization measurable. Comparing these two studies with the current one, a clear trend towards an improved scaffold handling and position stability is detectable. One explanation might be the implementation of 3D printing as a tool to improve the shape and fitting accuracy of scaffolds. The development of an under mild conditions plottable calcium phosphate paste was highly relevant for this achievement [10]. Nevertheless, the questions of scaffold geometry impact and relevance of a cell colonization needed to be answered for this new fabrication method applied in alveolar cleft models [12]. The previous *in vivo* comparison showed excellent osteoconductive properties of the 3D plotted calcium phosphate scaffolds with a significant influence of the pore geometry. The 60° pore geometry was superior compared to a 30° geometry regarding the remaining defect width and bone formation after 12 weeks. A colonization with undifferentiated rMSC before insertion did not enhance the defect healing in this study [12]. Irrespective of the geometry, in the previous study no resorption of the biomaterial within the experimental period occurred, but for a later clinical application in a growing organism this would be essential. Otherwise a tooth eruption or orthodontic movement into the grafted area won't be possible. This challenge might be overcome by the incorporation of MBG into the plottable CPC paste.

Histomorphologically, in this study an improved osseous integration of both (with/without HCM) composite scaffolds could be found and the quantitative results between the cSr and cSr-gCa(16) scaffolds showed a trend towards a smaller remaining defect width and pronounced bone formation. In comparison to the previous study with tissue engineered 3D printed bone grafts in this study the remaining defect widths were slightly higher (86.2% for the pure cSr and 85.1% for the cSr-gCa(16) scaffolds respectively) [12]. Explanation might be inter-individual variations between the rats and investigators of each study. A significant improvement of the defect ossification could be achieved by including the HCM into the MBG-particles. After 12 weeks the remaining defect width was 65.6% and the defect reduction occurred due to ongoing bone formation, which could be also confirmed by the significantly decreased distance between scaffold and defect margin. Descriptively, this group showed remarkable unilateral or bilateral osseous defect bridging, which was not present in the previous studies or for the other experimental groups [12,40,41]. In comparison to 3D bioprinted CPC scaffolds with the same 60° geometry [66], its combination with MBG and HCM was superior in terms of osseous defect healing. The improved cellular response *in vivo* is additionally substantiated by the *in vitro* cell seeding experiment. All three materials showed similar cell adhesion, but especially for the HCM-functionalized composite an enhanced cell proliferation was observed. The current study supports the idea of cell-free *in situ* tissue engineering approaches for reconstruction of critical size defects, because especially for large defects the nutrition of pre-seeded cells is challenging [67].

Alveolar clefts are part of the most common hereditary craniofacial anomaly in humans. 70% of the patients with cleft lip and/or palate suffer from a cleft alveolus and require bone grafting of the cleft area to stabilize the dental arch, close oronasal fistula and to enable an eruption of the permanent canine into the former cleft area [3,68]. Currently,

autologous bone grafts harvested from the iliac crest are applied to augment the hereditary segmental jawbone defect in a patient age of 9–11 years. This procedure is called "secondary alveolar cleft osteoplasty" and requires a second surgery site and might be associated with a donor site morbidity [33]. Besides the alveolar clefts, segmental alveolar bone defects can be result of traumas, odontogenic cysts, and tumors, which have in common that a functional and esthetic reconstruction requires bone grafts. The development of an autologous bone graft alternative is highly relevant to reduce donor site morbidity and the associated costs as well as to spare the patient from bone harvesting procedures [69,70].

Animal models are essential to evaluate new therapy concepts, which have *in vitro* confirmed their potential to improve the treatment quality of a hereditary disease. One drawback of small animal models like the current one is the impossibility to display all characteristics of a hereditary cleft. For example the shape of a human cleft is more irregular and sandglass-like leading to a higher initial bone to scaffold contact as it can be realized in the thin rat maxilla. This might have an impact on the bone formation beginning from the defect margins. Also postsurgical wound rest is difficult to archive in rats, whereas humans can be instructed accordingly and tools like nasal-gastral tubes are available to avoid chewing forces in the augmented cleft area.

Next step on the way to a clinical translation is an application in a large animal model of alveolar cleft osteoplasty, likewise to other tissue engineered bone grafts [71–73]. The *in vivo* evaluation of 3D printed scaffolds for this specific medical indication is comparably rare [74]. Nevertheless, the potential of customized, defect-specific bone grafts in alveolar cleft reconstruction and reconstructive oral surgery is obvious, but the number of clinical pilot studies evaluating 3D-printed bone grafts for alveolar osteoplasty is still limited [70,75,76]. There is one study by Ahn et al., who inserted successfully a 3D printed polycaprolactone scaffold, which was colonized with autologous MSC, in an adolescent. An osseous bridging of the defect occurred as well as the canine erupted spontaneously [77]. Nevertheless, the scaffold had to be fixed with an additional osteosynthesis and no conclusion was made about the degradation of the material. This in line with the conclusion of Salah et al. and Brézulier et al., who are highlighting the requirement of further research to identify the optimal material and technique for creating an alternative bone graft for alveolar cleft patients [70,75].

5. Conclusions

Cleft lip, alveolus and palate are the most common hereditary craniofacial anomalies in humans. Currently, the alveolar cleft is augmented using autologous bone grafts harvested from iliac crest of the particular patient. The procedure is called secondary alveolar cleft osteoplasty and is performed usually in a patient age of 9–11 years. The bone graft is associated with a donor site morbidity and limited availability by itself. The development of an alternative bone graft is highly relevant from a clinical point of view and the current study evaluated a new concept of 3D plotted bone scaffolds combined with the concept of *in situ* tissue engineering *in vitro* and *in vivo*. The implementation of MBG into a strontium-modified CPC paste improved the degradation rate in an alveolar cleft rat model significantly after 12 weeks. The scaffold degradation is essential, because clinically the bone graft needs to be replaced by autologous bone in a reasonable time to enable a tooth eruption in this area. Functionalizing the composite scaffolds with the secretome of hypoxia conditioned BM-MSCs led to a significantly improved bone formation rate *in vivo* compared to pure CPC or CPC-MBG scaffolds.

This underlines the potential of cell-free and defect-specific bone grafts for the augmentation of critical size defects like an alveolar cleft with the aim to improve the treatment quality of the mostly young patients. Moreover, an application of these functionalized bone grafts is also thinkable in osseous defects caused by other disease.

Ethics approval

The animal study was approved by the Commission for Animal Studies at the District Government Dresden, Germany (DD24- 5131/ 354/10).

CRediT authorship contribution statement

Richard Frank Richter: Conceptualization, Data curation, Formal analysis, Investigation, Methodology, Visualization, Writing – original draft, Writing – review & editing. **Corina Vater:** Formal analysis, Investigation, Methodology, Visualization, Writing – original draft, Writing – review & editing. **Margarete Korn:** Investigation, Visualization, Writing – review & editing. **Tilman Ahlfeld:** Conceptualization, Writing – review & editing. **Martina Rauner:** Investigation, Visualization, Writing – review & editing. **Winnie Pradel:** Investigation, Writing – review & editing. **Bernd Stadlinger:** Writing – review & editing. **Michael Gelinsky:** Funding acquisition, Project administration, Supervision, Writing – review & editing. **Anja Lode:** Conceptualization, Funding acquisition, Methodology, Project administration, Supervision, Writing – original draft, Writing – review & editing. **Paula Korn:** Conceptualization, Data curation, Formal analysis, Funding acquisition, Investigation, Methodology, Project administration, Supervision, Visualization, Writing – original draft, Writing – review & editing.

Declaration of competing interest

The authors declare no conflicts of interest.

Acknowledgments

Appendix A. Supplementary data

Supplementary data to this article can be found online at https://doi.org/10.1016/j.bioactmat.2023.06.001.

References

[1] R. Dimitriou, G.I. Mataliotakis, A.G. Angoules, N.K. Kanakaris, P.V. Giannoudis, Complications following autologous bone graft harvesting from the iliac crest and using the RIA: a systematic review, Injury 42 (2011) S3–S15, https://doi.org/10.1016/j.injury.2011.06.015.

[2] D.W. Hutmacher, Scaffolds in tissue engineering bone and cartilage, Biomaterials 21 (2000) 2529–2543, https://doi.org/10.1016/s0142-9612(00)00121-6.

[3] K.K.H. Gundlach, C. Maus, Epidemiological studies on the frequency of clefts in Europe and world-wide, J. Cranio-Maxillofacial Surg. 34 (2006) 1–2, https://doi.org/10.1016/s1010-5182(06)60001-2.

[4] H.H. Xu, P. Wang, L. Wang, C. Bao, Q. Chen, M.D. Weir, L.C. Chow, L. Zhao, X. Zhou, M.A. Reynolds, Calcium phosphate cements for bone engineering and their biological properties, Bone Res. 5 (2017), https://doi.org/10.1038/boneres.2017.56.

[5] W. Habraken, P. Habibovic, M. Epple, M. Bohner, Calcium phosphates in biomedical applications: materials for the future? Mater. Today 19 (2016) 69–87, https://doi.org/10.1016/j.mattod.2015.10.008.

[6] A. Bernhardt, M. Schumacher, M. Gelinsky, formation of osteoclasts on calcium phosphate bone cements and polystyrene depends on monocyte isolation conditions, Tissue Eng. C Methods 21 (2015) 160–170, https://doi.org/10.1089/ten.tec.2014.0187.

[7] E.B. Montufar, T. Traykova, E. Schacht, L. Ambrosio, M. Santin, J.A. Planell, M.-P. Ginebra, Self-hardening calcium deficient hydroxyapatite/gelatine foams for bone regeneration, J. Mater. Sci. Mater. Med. 21 (2009) 863–869, https://doi.org/10.1007/s10856-009-3918-7.

[8] Y. Maazouz, E.B. Montufar, J. Guillem-Marti, I. Fleps, C. Öhman, C. Persson, M.P. Ginebra, Robocasting of biomimetic hydroxyapatite scaffolds using self-setting inks, J. Mater. Chem. B 2 (2014) 5378–5386, https://doi.org/10.1039/c4tb00438h.

[9] A. Barba, A. Diez-Escudero, Y. Maazouz, K. Rappe, M. Espanol, E.B. Montufar, M. Bonany, J.M. Sadowska, J. Guillem-Marti, C. Öhman-Mägi, C. Persson, M.-C. Manzanares, J. Franch, M.-P. Ginebra, Osteoinduction by foamed and 3D-printed calcium phosphate scaffolds: effect of nanostructure and pore architecture, ACS Appl. Mater. Interfaces 9 (2017) 41722–41736, https://doi.org/10.1021/acsami.7b14175.

[10] S. Heinemann, S. Rössler, M. Lemm, M. Ruhnow, B. Nies, Properties of injectable ready-to-use calcium phosphate cement based on water-immiscible liquid, Acta Biomater. 9 (2013) 6199–6207, https://doi.org/10.1016/j.actbio.2012.12.017.

[11] A. Lode, K. Meissner, Y. Luo, F. Sonntag, S. Glorius, B. Nies, C. Vater, F. Despang, T. Hanke, M. Gelinsky, Fabrication of porous scaffolds by three-dimensional plotting of a pasty calcium phosphate bone cement under mild conditions, J. Tissue Eng. Regen. Med. 8 (2012) 682–693, https://doi.org/10.1002/term.1563.

[12] P. Korn, T. Ahlfeld, F. Lahmeyer, D. Kilian, P. Sembdner, R. Stelzer, W. Pradel, A. Franke, M. Rauner, U. Range, B. Stadlinger, A. Lode, G. Lauer, M. Gelinsky, 3D printing of bone grafts for cleft alveolar osteoplasty – in vivo evaluation in a preclinical model, Front. Bioeng. Biotechnol. 8 (2020), https://doi.org/10.3389/fbioe.2020.00217.

[13] T. Ahlfeld, T. Köhler, C. Czichy, A. Lode, M. Gelinsky, A methylcellulose hydrogel as support for 3D plotting of complex shaped calcium phosphate scaffolds, Gels 4 (2018) 68, https://doi.org/10.3390/gels4030068.

[14] A.R. Akkineni, Y. Luo, M. Schumacher, B. Nies, A. Lode, M. Gelinsky, 3D plotting of growth factor loaded calcium phosphate cement scaffolds, Acta Biomater. 27 (2015) 264–274, https://doi.org/10.1016/j.actbio.2015.08.036.

[15] M. Schumacher, A. Henß, M. Rohnke, M. Gelinsky, A novel and easy-to-prepare strontium(II) modified calcium phosphate bone cement with enhanced mechanical properties, Acta Biomater. 9 (2013) 7536–7544, https://doi.org/10.1016/j.actbio.2013.03.014.

[16] U. Thormann, S. Ray, U. Sommer, T. ElKhassawna, T. Rehling, M. Hundgeburth, A. Henß, M. Rohnke, J. Janek, K.S. Lips, C. Heiss, G. Schlewitz, G. Szalay, M. Schumacher, M. Gelinsky, R. Schnettler, V. Alt, Bone formation induced by strontium modified calcium phosphate cement in critical-size metaphyseal fracture defects in ovariectomized rats, Biomaterials 34 (2013) 8589–8598, https://doi.org/10.1016/j.biomaterials.2013.07.036.

[17] A. Lode, C. Heiss, G. Knapp, J. Thomas, B. Nies, M. Gelinsky, M. Schumacher, Strontium-modified premixed calcium phosphate cements for the therapy of osteoporotic bone defects, Acta Biomater. 65 (2018) 475–485, https://doi.org/10.1016/j.actbio.2017.10.036.

[18] S. Choudhary, P. Halbout, C. Alander, L. Raisz, C. Pilbeam, Strontium ranelate promotes osteoblastic differentiation and mineralization of murine bone marrow stromal cells: involvement of prostaglandins, J. Bone Miner. Res. 22 (2007) 1002–1010, https://doi.org/10.1359/jbmr.070321.

[19] E. Canalis, The divalent strontium salt S12911 enhances bone cell replication and bone formation in vitro, Bone 18 (1996) 517–523, https://doi.org/10.1016/8756-3282(96)00080-4.

[20] R. Baron, Y. Tsouderos, In vitro effects of S12911-2 on osteoclast function and bone marrow macrophage differentiation, Eur. J. Pharmacol. 450 (2002) 11–17, https://doi.org/10.1016/s0014-2999(02)02040-x.

[21] N. Takahashi, T. Sasaki, Y. Tsouderos, T. Suda, S 12911-2 inhibits osteoclastic bone resorption in vitro, J. Bone Miner. Res. 18 (2003) 1082–1087, https://doi.org/10.1359/jbmr.2003.18.6.1082.

[22] T. Ahlfeld, F.P. Schuster, Y. Förster, M. Quade, A.R. Akkineni, C. Rentsch, S. Rammelt, M. Gelinsky, A. Lode, 3D plotted biphasic bone scaffolds for growth factor delivery: biological characterization in vitro and in vivo, Adv. Healthc. Mater. 8 (2019), 1801512, https://doi.org/10.1002/adhm.201801512.

[23] L.L. Hench, J.R. Jones, Bioactive glasses: frontiers and challenges, Front. Bioeng. Biotechnol. 3 (2015), https://doi.org/10.3389/fbioe.2015.00194.

[24] C. Wu, J. Chang, Mesoporous bioactive glasses: structure characteristics, drug/growth factor delivery and bone regeneration application, Interface Focus 2 (2012) 292–306, https://doi.org/10.1098/rsfs.2011.0121.

[25] L.L. Hench, Bioceramics: from concept to clinic, J. Am. Ceram. Soc. 74 (1991) 1487–1510, https://doi.org/10.1111/j.1151-2916.1991.tb07132.x.

[26] J. Zhong, D.C. Greenspan, Processing and properties of sol-gel bioactive glasses, J. Biomed. Mater. Res. 53 (2000) 694–701, https://doi.org/10.1002/1097-4636(2000)53:6<694::aid-jbm12>3.0.co;2-6.

[27] M. Schumacher, L. Reither, J. Thomas, M. Kampschulte, U. Gbureck, A. Lode, M. Gelinsky, Calcium phosphate bone cement/mesoporous bioactive glass composites for controlled growth factor delivery, Biomater. Sci. 5 (2017) 578–588, https://doi.org/10.1039/c6bm00903d.

[28] R.F. Richter, T. Ahlfeld, M. Gelinsky, A. Lode, Development and characterization of composites consisting of calcium phosphate cements and mesoporous bioactive glass for extrusion-based fabrication, Materials 12 (2019) 2022, https://doi.org/10.3390/ma12122022.

[29] R.F. Richter, T. Ahlfeld, M. Gelinsky, A. Lode, Composites consisting of calcium phosphate cements and mesoporous bioactive glasses as a 3D plottable drug delivery system, Acta Biomater. (2022), https://doi.org/10.1016/j.actbio.2022.01.034.

[30] M.J. Dixon, M.L. Marazita, T.H. Beaty, J.C. Murray, Cleft lip and palate: understanding genetic and environmental influences, Nat. Rev. Genet. 12 (2011) 167–178, https://doi.org/10.1038/nrg2933.

[31] J.L. Moreau, J.F. Caccamese, D.P. Coletti, J.J. Sauk, J.P. Fisher, Tissue engineering solutions for cleft palates, J. Oral Maxillofac. Surg. 65 (2007) 2503–2511, https://doi.org/10.1016/j.joms.2007.06.648.

[32] P.D. Nguyen, C.D. Lin, A.C. Allori, J.L. Ricci, P.B. Saadeh, S.M. Warren, Establishment of a critical-sized alveolar defect in the rat: a model for human gingivoperiosteoplasty, Plast. Reconstr. Surg. 123 (2009) 817–825, https://doi.org/10.1097/prs.0b013e31819ba2f4.

[33] K.S. Boehm, M. Al-Taha, A. Morzycki, O.A. Samargandi, S. Al-Youha, M.R. LeBlanc, Donor site morbidities of iliac crest bone graft in craniofacial surgery, Ann. Plast. Surg. 83 (2018) 352–358, https://doi.org/10.1097/sap.0000000000001682.

[34] J. Rouwkema, N.C. Rivron, C.A. van Blitterswijk, Vascularization in tissue engineering, Trends Biotechnol. 26 (2008) 434–441, https://doi.org/10.1016/j.tibtech.2008.04.009.

[35] F.A. Auger, L. Gibot, D. Lacroix, The pivotal role of vascularization in tissue engineering, Annu. Rev. Biomed. Eng. 15 (2013) 177–200, https://doi.org/10.1146/annurev-bioeng-071812-152428.

[36] A. Gabrielyan, S. Knaak, M. Gelinsky, S. Arnhold, A. Rösen-Wolff, Hypoxia-conditioned media allows species-specific attraction of bone marrow stromal cells without need for recombinant proteins, BMC Vet. Res. 10 (2014), https://doi.org/10.1186/1746-6148-10-56.

[37] M. Quade, P. Münch, A. Lode, S. Duin, C. Vater, A. Gabrielyan, A. Rösen-Wolff, M. Gelinsky, The secretome of hypoxia conditioned hMSC loaded in a central depot induces chemotaxis and angiogenesis in a biomimetic mineralized collagen bone replacement material, Adv. Healthc. Mater. 9 (2019), 1901426, https://doi.org/10.1002/adhm.201901426.

[38] X. Yan, C. Yu, X. Zhou, J. Tang, D. Zhao, Highly ordered mesoporous bioactive glasses with superior in vitro bone-forming bioactivities, Angew. Chem. Int. Ed. 43 (2004) 5980–5984, https://doi.org/10.1002/anie.200460598.

[39] A. Ribeiro, M.M. Blokzijl, R. Levato, C.W. Visser, M. Castilho, W.E. Hennink, T. Vermonden, J. Malda, Assessing bioink shape fidelity to aid material development in 3D bioprinting, Biofabrication 10 (2017), 014102, https://doi.org/10.1088/1758-5090/aa90e2.

[40] P. Korn, M. Hauptstock, U. Range, C. Kunert-Keil, W. Pradel, G. Lauer, M.C. Schulz, Application of tissue-engineered bone grafts for alveolar cleft osteoplasty in a rodent model, Clin. Oral Invest. 21 (2017) 2521–2534, https://doi.org/10.1007/s00784-017-2050-1.

[41] P. Korn, M.C. Schulz, U. Range, G. Lauer, W. Pradel, Efficacy of tissue engineered bone grafts containing mesenchymal stromal cells for cleft alveolar osteoplasty in a rat model, J. Cranio-Maxillofacial Surg. 42 (2014) 1277–1285, https://doi.org/10.1016/j.jcms.2014.03.010.

[42] K. Donath, G. Breuner, A method for the study of undecalcified bones and teeth with attached soft tissues\ast. The Sage-Schliff (sawing and grinding) Technique, J. Oral Pathol. Med. 11 (1982) 318–326, https://doi.org/10.1111/j.1600-0714.1982.tb00172.x.

[43] C. Li, L. Gao, F. Chen, C. Liu, Fabrication of mesoporous calcium silicate/calcium phosphate cement scaffolds with high mechanical strength by freeform fabrication system with micro-droplet jetting, J. Mater. Sci. 50 (2015) 7182–7191, https://doi.org/10.1007/s10853-015-9244-1.

[44] A.-S. Wagner, M. Schumacher, M. Rohnke, K. Glenske, M. Gelinsky, S. Arnhold, S. Mazurek, S. Wenisch, Incorporation of silicon into strontium modified calcium phosphate bone cements promotes osteoclastogenesis of human peripheral mononuclear blood cells, Biomed. Mater. 14 (2019), 025004, https://doi.org/10.1088/1748-605x/aaf701.

[45] S.T. Moerz, P. Huber, pH-dependent selective protein adsorption into mesoporous silica, J. Phys. Chem. C 119 (2015) 27072–27079, https://doi.org/10.1021/acs.jpcc.5b09606.

[46] A. Gabrielyan, E. Neumann, M. Gelinsky, A. Rösen-Wolff, Metabolically conditioned media derived from bone marrow stromal cells or human skin fibroblasts act as effective chemoattractants for mesenchymal stem cells, Stem Cell Research &amp$\mathsemicolon$ Therapy 8 (2017), https://doi.org/10.1186/s13287-017-0664-5.

[47] H. Bretschneider, M. Quade, A. Lode, M. Gelinsky, S. Rammelt, S. Zwingenberger, K.-D. Schaser, C. Vater, Characterization of naturally occurring bioactive factor mixtures for bone regeneration, International Journal of Molecular Sciences 21 (2020) 1412, https://doi.org/10.3390/ijms21041412.

[48] A. Gabrielyan, M. Quade, M. Gelinsky, A. Rösen-Wolff, IL-11 and soluble VCAM-1 are important components of Hypoxia Conditioned Media and crucial for Mesenchymal Stromal Cells attraction, Stem Cell Research 45 (2020), 101814, https://doi.org/10.1016/j.scr.2020.101814.

[49] D.I. Holmes, I. Zachary, The vascular endothelial growth factor (VEGF) family: angiogenicfactors in health and disease, Genome Biology 6 (2005) 209, https://doi.org/10.1186/gb-2005-6-2-209.

[50] K.A. Fitzgerald, L.A.J. O'Neill, A.J.H. Gearing, R.E. Callard, VEGF, in: the Cytokine FactsBook and Webfacts, Elsevier, 2001, pp. 498–504, https://doi.org/10.1016/b978-012155142-1/50108-1.

[51] B. Chaqour, Regulating the regulators of angiogenesis by CCN1 and taking it up a Notch, Journal of Cell Communication and Signaling 10 (2016) 259–261, https://doi.org/10.1007/s12079-016-0328-8.

[52] L.A. Bach, Recent insights into the actions of IGFBP-6, Journal of Cell Communication and Signaling 9 (2015) 189–200, https://doi.org/10.1007/s12079-015-0288-4.

[53] A. Walia, J.F. Yang, Y. Huang, M.I. Rosenblatt, J.-H. Chang, D.T. Azar, Endostatin's emerging roles in angiogenesis, lymphangiogenesis, disease, and clinical applications, Biochimica et Biophysica Acta (BBA) - General Subjects 1850 (2015) 2422–2438, https://doi.org/10.1016/j.bbagen.2015.09.007.

[54] K.-H. Chang, T. Chan-Ling, E.L. McFarland, A. Afzal, H. Pan, L.C. Baxter, L.C. Shaw, S. Caballero, N. Sengupta, S.L. Calzi, S.M. Sullivan, M.B. Grant, IGF binding protein-3 regulates hematopoietic stem cell and endothelial precursor cell function

[55] J.L. Kielczewski, Y.P.R. Jarajapu, E.L. McFarland, J. Cai, A. Afzal, S.L. Calzi, K.H. Chang, T. Lydic, L.C. Shaw, J. Busik, J. Hughes, A.J. Cardounel, K. Wilson, T.J. Lyons, M.E. Boulton, R.N. Mames, T. Chan-Ling, M.B. Grant, Insulin-like growth factor binding protein-3 mediates vascular repair by enhancing nitric oxide generation, Circulation Research 105 (2009) 897–905, https://doi.org/10.1161/circresaha.109.199059.

[56] M. Deng, K. Luo, T. Hou, F. Luo, Z. Xie, Z. Zhang, A. Yang, B. Yu, S. Yi, J. Tan, S. Dong, J. Xu, IGFBP3 deposited in the human umbilical cord mesenchymal stem cell-secreted extracellular matrix promotes bone formation, Journal of Cellular Physiology 233 (2018) 5792–5804, https://doi.org/10.1002/jcp.26342.

[57] F. Perut, E.B. Montufar, G. Ciapetti, M. Santin, J. Salvage, T. Traykova, J.A. Planell, M.P. Ginebra, N. Baldini, Novel soybean/gelatine-based bioactive and injectable hydroxyapatite foam: material properties and cell response, Acta Biomaterialia 7 (2011) 1780–1787, https://doi.org/10.1016/j.actbio.2010.12.012.

[58] S. del Valle, N. Miño, F. Muñoz, A. González, J.A. Planell, M.-P. Ginebra, In vivo evaluation of an injectable macroporous calcium phosphate cement, Journal of Materials in Medicine 18 (2007) 353–361, https://doi.org/10.1007/s10856-006-0700-y.

[59] J. Konka, J. Buxadera-Palomero, M. Espanol, M.-P. Ginebra, 3D printing of hierarchical porous biomimetic hydroxyapatite scaffolds: adding concavities to the convex filaments, Acta Biomaterialia 134 (2021) 744–759, https://doi.org/10.1016/j.actbio.2021.07.071.

[60] R.A. Perez, H.-W. Kim, M.-P. Ginebra, Polymeric additives to enhance the functional properties of calcium phosphate cements, Journal of Tissue Engineering 3 (2012), 204173141243955, https://doi.org/10.1177/2041731412439555.

[61] A. Shimatani, H. Toyoda, K. Orita, Y. Ibara, Y. Yokogawa, H. Nakamura, A bone replacement-type calcium phosphate cement that becomes more porous in vivo by incorporating a degradable polymer, Journal of Materials Science: Materials in Medicine 32 (2021), https://doi.org/10.1007/s10856-021-06555-1.

[62] J.R. Jones, Review of bioactive glass: from Hench to hybrids, Acta Biomaterialia 9 (2013) 4457–4486, https://doi.org/10.1016/j.actbio.2012.08.023.

[63] D. Kilian, T. Ahlfeld, A.R. Akkineni, A. Bernhardt, M. Gelinsky, A. Lode, 3D Bioprinting of osteochondral tissue substitutes – in vitro-chondrogenesis in multi-layered mineralized constructs, Scientific Reports 10 (2020), https://doi.org/10.1038/s41598-020-65050-9.

[64] F. Liang, H. Leland, B. Jedrzejewski, A. Auslander, S. Maniskas, J. Swanson, M. Urata, J. Hammoudeh, W. Magee, Alternatives to autologous bone graft in alveolar cleft reconstruction, Journal of Craniofacial Surgery 29 (2018) 584–593, https://doi.org/10.1097/scs.0000000000004300.

[65] B.J. Mehrara, P.B. Saadeh, D.S. Steinbrech, M. Dudziak, B.H. Grayson, C.B. Cutting, J.G. McCarthy, G.K. Gittes, M.T. Longaker, A rat model of gingivoperiosteoplasty, Journal Of Craniofacial Surgery 11 (2000) 54–58, https://doi.org/10.1097/00001665-200011010-00010.

[66] T. Ahlfeld, A. Lode, R.F. Richter, W. Pradel, A. Franke, M. Rauner, B. Stadlinger, G. Lauer, M. Gelinsky, P. Korn, Toward biofabrication of resorbable implants consisting of a calcium phosphate cement and fibrin—a characterization in vitro and in vivo, International Journal of Molecular Sciences 22 (2021) 1218, https://doi.org/10.3390/ijms22031218.

[67] J.L. Ricci, E.A. Clark, A. Murriky, J.E. Smay, Three-dimensional printing of bone repair and replacement materials, Journal of Craniofacial Surgery 23 (2012) 304–308, https://doi.org/10.1097/scs.0b013e318241dc6e.

[68] B.B. Horswell, J.M. Henderson, Secondary osteoplasty of the alveolar cleft defect, Journal of Oral and Maxillofacial Surgery 61 (2003) 1082–1090, https://doi.org/10.1016/s0278-2391(03)00322-7.

[69] M.-L. Mueller, J.R. Thamm, M.J. Troulis, F.P.S. Guastaldi, Clinical application of three dimensional printing and tissue engineering for maxillofacial reconstruction. A review of reported cases, JSM Oro Facial Surgeries 4 (2020) 1013.

[70] M. Salah, L. Tayebi, K. Moharamzadeh, F.B. Naini, Three-dimensional bio-printing and bone tissue engineering: technical innovations and potential applications in maxillofacial reconstructive surgery, Maxillofacial Plastic and Reconstructive Surgery 42 (2020), https://doi.org/10.1186/s40902-020-00263-6.

[71] N. Pourebrahim, B. Hashemibeni, S. Shahnaseri, N. Torabinia, B. Mousavi, S. Adibi, F. Heidari, M.J. Alavi, A comparison of tissue-engineered bone from adipose-derived stem cell with autogenous bone repair in maxillary alveolar cleft model in dogs, International Journal of Oral and Maxillofacial Surgery 42 (2013) 562–568, https://doi.org/10.1016/j.ijom.2012.10.012.

[72] M. Yoshioka, K. Tanimoto, Y. Tanne, K. Sumi, T. Awada, N. Oki, M. Sugiyama, Y. Kato, K. Tanne, Bone regeneration in artificial jaw cleft by use of carbonated hydroxyapatite particles and mesenchymal stem cells derived from iliac bone, International Journal of Dentistry 2012 (2012), https://doi.org/10.1155/2012/352510, 1–8.

[73] D. Zhang, F. Chu, Y. Yang, L. Xia, D. Zeng, H. Uludağ, X. Zhang, Y. Qian, X. Jiang, Orthodontic Tooth Movement in Alveolar Cleft Repaired with a Tissue Engineering Bone: An Experimental Study in Dogs, Tissue Engineering Part A 17 (2011) 1313–1325, https://doi.org/10.1089/ten.tea.2010.0490.

[74] R.R. Ibáñez, N.C. Mateo, L.M. Rodríguez-Lorenzo, A. Rodríguez-Navarrete, M.O.L. Flores-Sánchez, Potential benefits from 3D printing and dental pulp stem cells in cleft palate treatments: an in vivo model study, Biomedical Journal of Scientific &amp$\mathsemicolon$ Technical Research 16 (2019), https://doi.org/10.26717/bjstr.2019.16.002831.

[75] D. Brézulier, L. Chaigneau, S. Jeanne, R. Lebullenger, The challenge of 3D bioprinting of composite natural polymers PLA/bioglass: trends and benefits in

cleft palate surgery, Biomedicines 9 (2021) 1553, https://doi.org/10.3390/biomedicines9111553.

[76] L.P. Hatt, K. Thompson, J.A. Helms, M.J. Stoddart, A.R. Armiento, Clinically relevant preclinical animal models for testing novel cranio-maxillofacial bone 3D-printed biomaterials, Clinical and Translational Medicine 12 (2022), https://doi.org/10.1002/ctm2.690.

[77] G. Ahn, J.-S. Lee, W.-S. Yun, J.-H. Shim, U.-L. Lee, Cleft alveolus reconstruction using a three-dimensional printed bioresorbable scaffold with human bone marrow cells, Journal of Craniofacial Surgery 29 (2018) 1880–1883, https://doi.org/10.1097/scs.0000000000004747.